Head and Neck Lymph Node Region Delineation with Automatic Segmentation and Image Registration

Chia-Chi Teng

A dissertation
submitted in partial fulfillment of the
requirement for the degree of

Doctor of Philosophy

University of Washington

2007

Program Authorized to Offer Degree:
Department of Electrical Engineering

University of Washington
Graduate School

This is to certify that I have examined this copy of a doctoral dissertation by

Chia-Chi Teng

and have found that it is complete and satisfactory in all respects,
and that any and all revisions required by the final
examining committee have been made.

Chair of the Supervisory Committee:

Linda G. Shapiro

Reading Committee:

Linda G. Shapiro

Ira J. Kalet

James F. Brinkley III

Date: April 6, 2007

In presenting this dissertation in partial fulfillment of the requirements for the Doctoral degree at the University of Washington, I agree that the Library shall make its copies freely available for inspection. I further agree that extensive copying of the dissertation is allowable only for scholarly purposes, consistent with "fair use" as prescribed in the U.S. Copyright Law. Requests for copying or reproduction of this dissertation may be referred to Proquest Information and Learning, 300 North Zeeb Road, P.O. Box 1346, Ann Arbor, MI 48106-1346, to whom the author has granted "the right to reproduce and sell (a) copies of the manuscript in microform and/or (b) printed copies of the manuscript made from microform."

Signature Chi-Chi Zhang

Date 5/7/2007

University of Washington

Abstract

Head and Neck Lymph Node Region Delineation
with Automatic Segmentation and Image Registration

Chia-Chi Teng

Chair of the Supervisory Committee
Professor Linda G. Shapiro
Department of Electrical Engineering
and Department of Computer Science and Engineering

The success of radiation therapy depends critically on accurately delineating the target volume, which is the region of known or suspected disease in a patient. Methods that can compute a contour set defining a target volume on a set of patient images will contribute greatly to the success of radiation therapy and dramatically reduce the workload of radiation oncologists, who currently draw the target by hand on the images using simple computer drawing tools. The most challenging part of this process is to estimate where there is microscopic spread of disease.

We are developing methods for automatically selecting and adapting standardized regions of tumor spread based on the location of lymph nodes in a standard or reference case, together with image segmentation and registration techniques. Previously available techniques appear promising but can be supplemented by anatomic knowledge and landmark-based methods to achieve a clinically acceptable match.

TABLE OF CONTENTS

LIST OF FIGURES

LIST OF TABLES

Chapter 1 Introduction

Malignant tumors in the head and neck represent a great epidemiological problem in western countries. Head and neck cancer accounts for approximately 3% of all cancer cases reported in the United State, or roughly 50,000 cases per year [1]. Due to the tumor position, the risk of developing lymph node metastases in the neck region is very high. Radiation therapy will be used as part of the treatment in a majority of the cases. Therefore a fast and effective system for creating a conformal radiation treatment of enlarged (i.e. potentially malignant) lymph nodes is essential.

1.1 Conformal Radiation Therapy

Traditionally, the planning of radiation treatments has been done in two dimensions (width and height). Conformal radiation therapy is a procedure that uses computer technology to create a 3-dimentional image of the tumor, which allows doctors to give the highest possible does of radiation to the tumor, while sparing the normal tissue as much as possible. A 3D image of a tumor can be obtained using computed tomography (CT), magnetic resonance imaging (MRI), positron emission tomography (PET), or single photon emission computed tomography (SPECT). Using information from the image, special computer programs design radiation beams that "conform" to the shape of the tumor. Because the healthy tissue surrounding the tumor is largely spared by this technique, higher doses of radiation can be used to treat the cancer. Improved outcomes with 3D conformal radiation therapy have been reported for nasopharyngeal, prostate, lung, liver, and brain cancers.

1.2 Intensity Modulated Radiation Therapy

Intensity Modulated Radiation Therapy (IMRT) is a new type of 3–D conformal radiation therapy that uses radiation beams (usually x-rays) of varying intensities to deliver different doses of radiation to small areas of tissue at the same time. The technology allows for the delivery of higher doses of radiation within the tumor and lower doses to nearby healthy tissue. Some techniques deliver a higher dose of radiation to the patient each day, potentially shortening the overall treatment time and improving the success of the treatment. IMRT may also lead to fewer side effects during treatment.

The radiation is delivered by a linear accelerator that is equipped with a multileaf collimator (a collimator helps to shape or sculpt the beams of radiation). The equipment can be rotated around the patient so that radiation beams can be sent from the best angles. The beams conform as closely as possible to the shape of the tumor. Because IMRT equipment is highly specialized, not every radiation oncology center uses IMRT.

This new technology has been used to treat tumors in the brain, head and neck, nasopharynx, breast, liver, lung, prostate, and uterus. However, IMRT is not appropriate or necessary for every patient or tumor type. Long-term results following treatment with IMRT are becoming available. However, the success of this strategy depends on knowing the exact extent of the target volume in each patient.

1.3 Clinical Target Volumes

Computerized tomography (CT) scanning is commonly used for conformal radiation treatment, and the scan is performed with the patient set in his treatment position, immobilized using custom devices, thereby minimizing movement of the treatment target. Radiation oncologists have adopted definitions for the various components of the target volume, in order to achieve some uniformity and facilitate the conduct of inter institutional clinical trials [8], [9]. The Gross Target Volume (GTV) is the visible and palpable tumor mass. Although it can usually be seen on images (CT and MR), it is normally difficult to automatically identify with existing image processing techniques. To date it is still usually hand drawn by clinicians using a computer drawing software tool. The Clinical Target Volume (CTV) includes the locations of microscopic local and regional spread, which usually means the GTV plus the lymph node regions around it. Microscopic disease cannot currently be imaged by any existing technique. Even the nodes themselves are often hard to identify in the images. The task of delineating these nodal regions, which is also usually done by the clinicians, is quite time consuming. Figure 1 shows how these target volumes are related to each other.

Clinicians often elect to perform less aggressive treatment, because they do not have the time to draw the detail outlines of the nodal regions and CTV, even if they are confident of which node groups are likely to have disease to treat.

With a well-designed 3D radiation therapy plan, critical anatomical structures can be avoided, while radiation dosage is maximized for the lymph node region. As imaging based cervical lymph node region classification is developed [2], a system that can identify those critical anatomical structures by segmenting patients' CT

images with little or no user interaction is crucial to the success of implementing a fast and effective radiation treatment planning system.

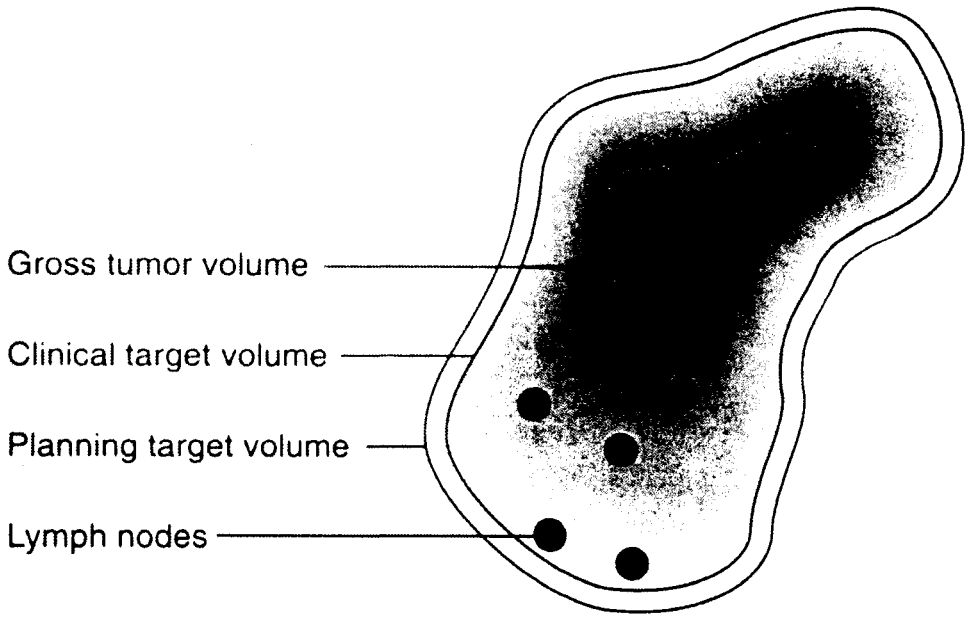

Figure 1: Illustration of target volumes. (Courtesy of Mary Austin-Seymour [66])

1.4 Motivation

Creating the 3D clinical target volume (CTV) is a critical part of the 3D radiation treatment and IMRT. The success of radiotherapy depends critically on the accuracy of the CTV. As 3D conformal radiotherapy and IMRT become the state of the art, the process of CTV delineation is more important than ever. This process currently requires radiation oncologists to manually draw the 2D target contours on axial CT slices. It is tedious, time consuming and can be the bottle neck to make IMRT available to more patients. Software tools that automate the segmentation of landmark structures and contouring of target volume can

dramatically decrease the planning effort for radiation oncologists and increase the availability of IMRT to more patients and the success rate of radiotherapy.

1.5 System Overview

This prototype system will take a cancer patient's head and neck CT images and produce projections of lymph node regions, which can be used to produce a clinical target volume (CTV) for the radiation treatment plan. The system can be divided into the following major components:

- Segmentation,
- Retrieval of similar reference models,
- Image registration.

Figure 2 shows a block diagram of how these components are linked. The offline process on the left creates a database ***DB*** of CT scans from prototypical reference patients on which experts have drawn contours that denote the lymph regions. These reference images $\{\boldsymbol{d}_i\}$ are segmented offline to extract 3D volumes of landmark anatomical structures such as the mandible and hyoid [58]. 3D meshes and geometric properties of these 3D volumes are also stored in the database.

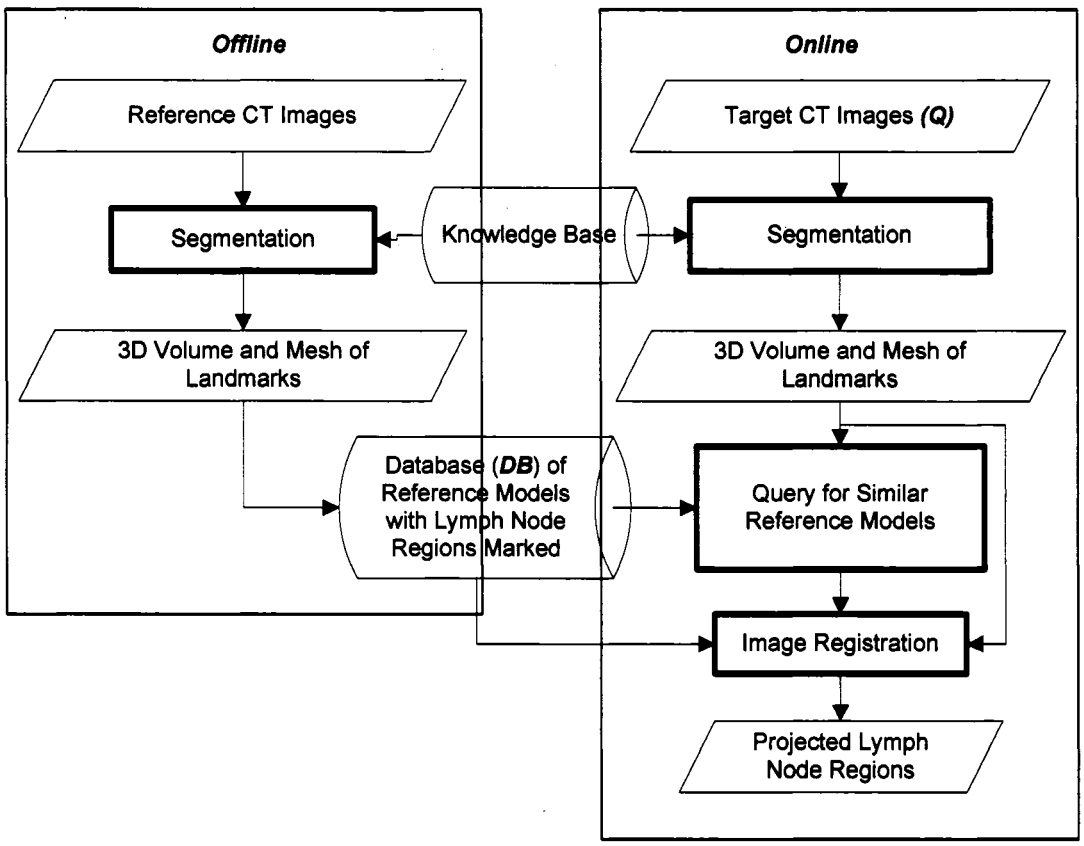

Figure 2: System components block diagram.

A target patient's CT image is also segmented to extract landmark anatomical structures during the online process as shown in Figure 2. Given a single query CT scan $\boldsymbol{Q}$ from a target patient; we need to have a fast and effective way to determine the similarity between $\boldsymbol{Q}$ and each database image $\boldsymbol{d}$ in $\boldsymbol{DB}$ in order to find the most similar database images $\{\boldsymbol{d_s}\}$. We will use the images from the query result as reference models for the 3D deformable image registration procedure [57], which is much more computationally complex and time consuming. The image registration procedure produces a transformation between the reference and target images which can be used to generate projected lymph node regions for the target patient.

This thesis is organized as follows. In Chapter 2 we review the background and related research. Chapter 3 describes the image registration method that utilizes 3D landmark correspondence and the process of applying boundary constraints to refine the projected lymph node regions. Chapter 4 discusses the segmentation component in detail. The retrieval process of similar reference models is discussed in Chapter 5.

The work we report here was conducted using the Prism radiation therapy planning system [10] not only to take advantage of the drawing tools in Prism, but also to eventually be able to test the method with a series of clinical cases and to ultimately put it into direct clinical use.

Chapter 2 Background and Related Research

2.1 Nodal Region Reference Model

The neck has an extensive lymphatic network [5]. In fact, more than one third of the body's total number of lymph nodes resides in the extracranial head and neck. Cervical lymph nodes are divided into regions or 'levels' that are described by their anatomical location [3]. Although this traditional classification was decided using surgical landmarks, translation into an imaging-based nodal classification is feasible. Figure 3 is a diagram of the lymph nodes in the head and neck.

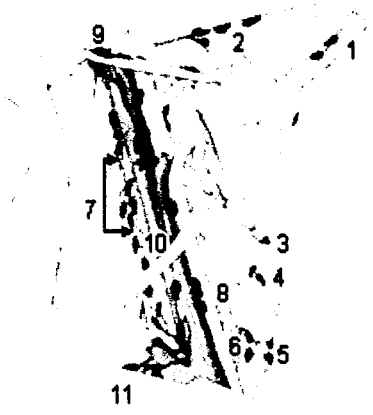

Figure 3: Cervical lymph nodes. (Image from Wikipedia, public domain work)

Som *et al.* [11][12] undertook a study to create an imaging-based classification for the lymph nodes of the neck that can be accepted by clinicians and easily used by radiologists. Imaging anatomic landmarks were chosen to create a consistent nodal classification similar to the clinically-based classifications. Radiologists must be able to identify the pertinent anatomic landmarks such as the bottom of the hyoid bone, the back edge of the submandibular gland, and the back

edge of the sternocleidomastoid muscle. Table 1 shows a summary of such classifications.

We chose a patient to serve as a reference model for creating the standard regions. At this stage the reference model is an arbitrary data set. In the course of this work, we expect to determine criteria for an optimal reference model. We used the Prism [10] system to create a series of contoured volumes representing the nodal regions on the reference model. With the Prism volume editor, we created 2D contours for all the nodal levels on each relevant axial image. Hence the nodal regions are defined as a series of 2D contours in the 3D space. Figure 4 shows one of the axial images with contours of the level IA, IB, II, and V nodal regions. Figure 5 shows the contours of the nodal regions in a 3D view.

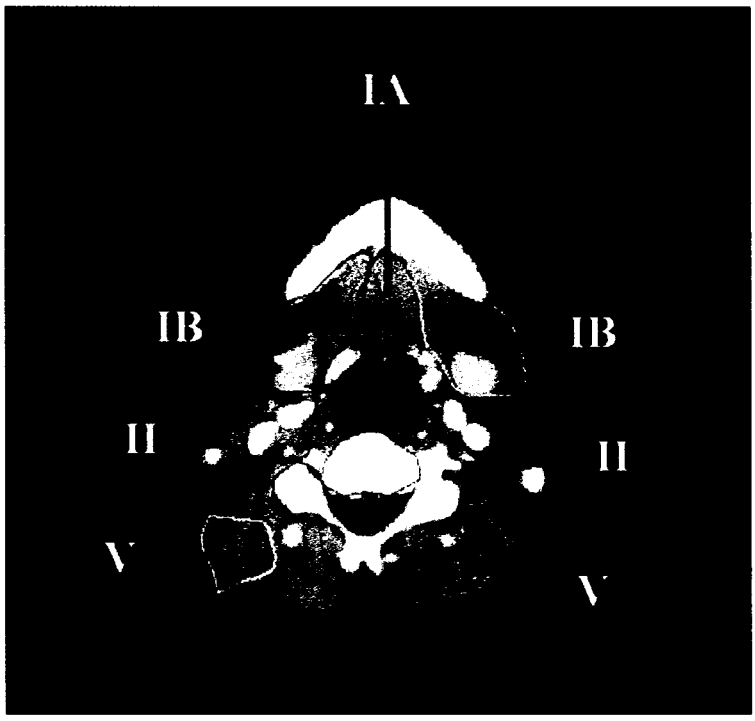

Figure 4: Nodal region contours of a reference model.

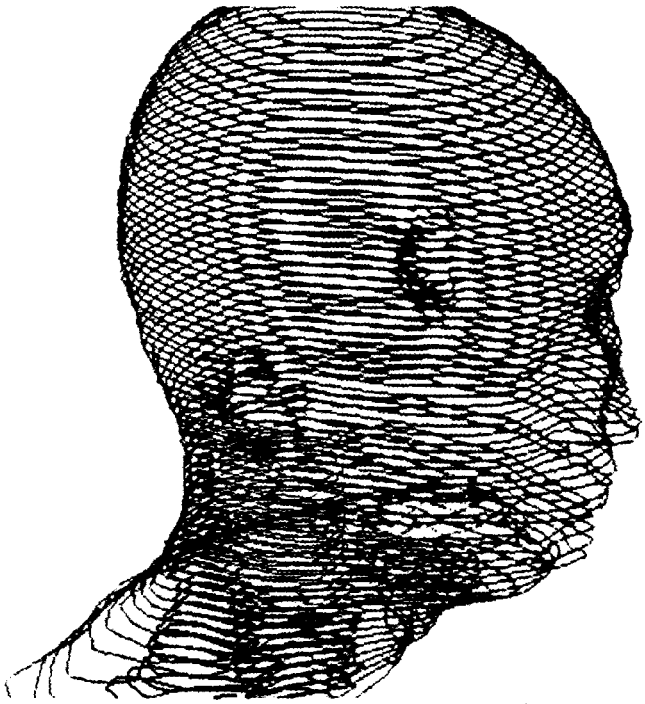

Figure 5: Contours of nodal regions in 3D view.

Table 1: Imaging-based neck nodal classification.

Level I	Submental and submandibular nodes.
Level I A	Submental nodes, between the medial margins of the anterior bellies of the digastric muscles.
Level I B	Submandibular nodes, lateral to level I A nodes and anterior to the back of the submandibular salivary gland.
Level II	Upper internal jugular nodes, posterior to the back of the submandibular salivary gland, anterior to the back of the sternocleidomastoid muscle and above the level of the bottom of the body of the hyoid bone.
Level III	Middle jugular nodes, between the level of the bottom of the body of the hyoid bone and the level of the bottom of the cricoid arch, anterior to the back of the sternocleidomastoid muscle.
Level IV	Low jugular nodes, between the level of the bottom of the cricoid arch and the level of the clavicle, anterior to a line connecting the back of the sternocleidomastoid muscle and the posterolateral margin of the anterior scalene muscles; they are lateral to the carotid arteries.
Level V	Posterior triangle nodes, posterior to the back of the sternocleidomastoid muscle, and posterior to the line described in level IV.
Level V A	Above the level of the bottom of the cricoid arch.
Level V B	Between the level of the bottom of the cricoid arch and the level of the clavicle.
Level VI	Upper visceral nodes, between the carotid arteries from the level of the bottom of the body of the hyoid bone to the level of the top of the manubrium.
Level VII	Superior mediastinal nodes, between the carotid arteries below the level of the top of the manubrium and above the innominate vein.
Supraclavicular nodes	Nodes at, or caudal to, the level of the clavicle and lateral to the carotid artery.
Retropharyngeal nodes	Nodes behind the pharynx, medial to the internal carotid artery, from the skull base down to the level of the hyoid bone.

2.2 Knowledge-based Segmentation

The research of knowledge-based medical image analysis existed long before the use of CT images in common clinical practice. Early studies used knowledge-based image analysis on radiographic image segmentation before CT imaging was commonly available in hospitals [13] [14]. Karssemeijer *et al.* [15] made effective use of domain knowledge incorporated in a semantic network of spatial relations among organs. Brinkley [16] used a geometric constraint network approach to segmentation of CT images. Kobashi and Shapiro [17] proposed a knowledge-based method using constraint-based dynamic thresholding, negative shape constraints, and progressive landmarking.

Most recent knowledge-based segmentation studies are based on the following models,

- intensity models that describe the gray-level appearance of individual structures,
- shape models that describe the shape of structure in a given population, and
- geometric models that describe the spatial relationships between structures in a given population.

Automatic segmentation algorithms often use some form of intensity models to describe the gray-level appearance of anatomical structures. Shape models are an active research area in medical imaging, for example, parametric models [18], deformable models [19], and principle component analysis (PCA) methods can be found in the recent literature. While deformable models incorporate constraints of local smoothness, principle components restrict global constraints as they capture the directions of largest variation in a given set of points. Szekely *et al.* [20] used a method derived from a combination of deformable model and principle component

analysis. Rough geometric models were used by Kobashi and Shapiro for their progressive landmarking as a "coarse to fine" strategy for segmentation in which the easily identifiable or coarse structures are first segmented automatically, and their geometry is then used to bootstrap the segmentation of other fine structures that are harder to locate.

2.3 Image Registration

Image registration is commonly used in medical imaging applications. It is essentially a process of finding a geometric transformation **g** between two sets of images, which maps a point **x** in one image-based coordinate system to **g(x)** in the other. By assuming the head and neck anatomy has similar characteristics between a specific patient and a reference person, we can use image registration methods to transform a region from the reference image set to the patient image set.

2.3.1 Classification

Maintz and Viergever classified different image registration methods based on different criteria and levels [21]. For example, by the nature of the registration basis, there are the following different image registration methods:

1. Landmark-based methods
    a. Anatomical
    b. Geometrical
2. Segmentation-based methods
    a. Rigid models (points, curves, surfaces)
    b. Deformable models (snakes, nets)
3. Voxel-property-based methods
    a. Reduction to scalars/vectors (moments, principle axes)

b. Using full image content (cross-correlation, mutual information)

By the nature of the transformation, the registration can be based on rigid, affine, or deformable transformations. By the modalities involved, there are monomodal or multimodal registration. By the subjects (patients) involved, there are intrasubject, intersubject or atlas registration. While intrasubject, multimodal, rigid transformation methods are more commonly used for other radiotherapy treatment applications; this proposal focuses on intersubject registration, which appears mostly in brain image applications. In order to achieve better results for intersubject registration, it is necessary to use deformable transformations.

Registration of both intrasubject and intersubject brain images has been the subject of extensive study in the medical imaging literature. Research based on various methods is discussed below.

2.3.2 Landmark-based registration methods

Landmark-based registration methods use anatomical or geometrical landmark points to match the image properties in different data sets and bring them into alignment. Anatomical landmarks are locatable points of the morphology of the visible anatomy, usually identified interactively by user. Geometrical landmarks are points at the locus of some geometric property, e.g. local curvature extrema, corners, etc. Technically, the identification of landmark points is a segmentation procedure, but the classification of segmentation-based registration is normally reserved for methods relating to segmentation of structures of higher order, i.e. curves, surfaces, and volumes. Landmark-based methods are generally used to find rigid or affine transformations. However, if the sets of points are large enough, they can be used for more complex, or non-rigid transformations.

Algorithms were developed to optimize measures such as average distance between each landmark and its closest counterpart (the Procrustean metric), or iterated minimal landmark distances. For the optimization of the latter measure, the iterative closest point (ICP) algorithm [22] and derived methods are popular because of their versatility, computational speed and ease of implementation.

Bookstein [23] uses landmark points to define thin-plate splines (TPS) that can be deformed to match the corresponding homologous landmarks in two different image sets, and other applications [24] have also been developed using similar methods. Landmark points are used to determine the coefficients of the polynomial using linear regression. These landmark-based methods generally require extensive user interaction to define a large number of landmark points for better results.

Anatomical landmarks are also often used in combination with an entire different registration basis, the following paradigms being used for brain mapping: Christensen *et al.* [25] use interactive methods to locate anatomical landmarks that define Frankfort Horizontal plane, the Median Sagittal Plane, and the Coronal Plane; these planes are then used to estimate the rigid registration before running non-rigid registration with a different method (elastic model). Christensen *et al.* [26] require user input to define major sulcal lines in both template and target data sets. Each line was parameterized by an ordered set of points, which were then used to create an initial affine transformation. The initial transformation was later concatenated with a non-rigid elastic and fluid-based transformation.

Thompson and Toga [27] use manually-defined points on the surfaces of the lateral ventricles and on the cerebral cortex to construct initial surface models that

are later used to register surface and volumetric warp. Note that the exact location and distribution of these manually defined points is not critical, since they are only used to fit an initial surface estimate. Moreover, the points picked in two data sets need not be homologous, nor do they need to correspond to known functional landmarks.

Davatzikos created a deformable surface model with curvature information of the cortical surface [28]. Based on the curvature map, a number of sulci and fissures are identified manually from the minimum and maximum curvatures [29, 30]. The sulcal surfaces are then parameterized and matched with a 3D elastic warp.

2.3.3 Segmentation-based registration methods

Segmentation-based registration methods use various segmentation techniques to extract geometrical features, e.g. surfaces of the cortex, which can be used to align different images. Like landmark-based methods, they require an additional step to extract image features such as 2D boundaries or 3D surfaces, using either labor-intensive manual methods or complicated (semi-) automatic methods.

A general drawback of segmentation-based rigid registration is that the registration accuracy is limited to the accuracy of the segmentation process. Furthermore, deformable models often need a good initial position in order to properly converge; this is generally realized by user interaction. Another disadvantage is that the local deformation of the template can often be unpredictably erratic, if the target structure differs sufficiently from the template structure.

Thompson and Toga [27] use a surface-based technique for warping 3D images of the brain. They first model cortical and major sulcal surfaces as active 3D surface meshes and calculate the surface warp among corresponding surfaces between different data set. The volume warp is calculated by interpolating the surface warps. Davatzikos *et al.* [30, 31] use a threshold-based, seeded region-growing method, in conjunction with erosion and a conditional dilation operation to determine the initial outer cortical surfaces. Then an active contour algorithm is used to establish a homothetic one-to-one map between a set of region boundaries in two images to be registered. This mapping is finally used to create the elastic spatial transformation.

2.3.4 Voxel-property-based registration methods

The voxel-property-based methods directly use the voxel properties, e.g. voxel intensity, to match the reference and target images. Unlike landmark-based and segmentation-based methods, they do not require an additional step to extract image properties, a major advantage. Various similarity measures were used to register the voxel properties:

- cross-correlation [33, 34],
- maximization of mutual information [33, 34], and
- minimization of the absolute or squared intensity differences [25, 26, 35].

Christensen *et al.* [26, 35] use elastic solids and viscous fluids to model the image data, with an intensity-based approach to compare an atlas and a target scan. Although the results of this method are impressive, the computation time is very long, and massively parallel computers are needed to solve complicated partial differential equations. Furthermore, the elasticity or viscosity coefficients need to be optimized with additional extensive computation. Kjems *et al.* [34] use both

cross-correlation and mutual information measures as global cost functions for intersubject PET image registration. Although voxel-property-based methods have been around a long time, their uses in extensive 3D-3D clinical applications have been limited by the considerable computational costs.

2.3.5 Mutual information methods

Mutual information is an entropy-based measure of image alignment derived from probabilistic measures of image intensity values [24, 28] and has been used in many intrasubject, multimodal applications. According to the principle of mutual information, homogeneous regions of the first image set should generally map into homogeneous regions in the second set. Maes *et al.* [38] and Viola and Wells [39] use the maximization of mutual information to align 3D image sets of different modalities.

One major drawback of mutual information as it is commonly used is the absence of spatial information in the measure, i.e. the dependence of the grey values of the neighboring voxels is ignored. The following methods were suggested to incorporate the dependence of the grey values of neighboring voxels, or spatial information of the images, to improve the registration. Studholme *et al.* [22] compute the mutual information of two images together with a labeling of one of the images. It requires additional segmentation and labeling steps, and the quality of the resulting labeled regions is a big factor in this approach. For the head and neck images, it can be difficult to create consistent and usable labels with an automatic scheme. Pluim *et al* [32] combine mutual information with an additional term based on the image gradient of the images to be registered. Although the robustness of this approach is yet to be proven, it has encouraging initial results

which warrant further investigation, particularly on a mono-modal registration application like ours.

2.3.6 Physical model vs. free-form deformation

Physical-model-based warping methods have the advantage of a smooth transformation, which tends to preserve the relative positions of anatomical structures while offering a high flexibility to allow for considerable intersubject variability. These physical models are developed based on actual physical materials, e.g. elastic surfaces, instead of biology; hence they do not always correctly represent human anatomy. Additional knowledge or experiments are required to determine the optimal elasticity or viscosity coefficients.

Thompson and Toga [27] model the cortical and sulcal surfaces as elastic surfaces that deform according to the external and internal forces. Davatzikos *et al.* [30, 31] use a similar active contour algorithm to deform the outer cortical surfaces as elastic surfaces. Christensen *et al.* [26, 35] use elastic solids and viscous fluids with different visco-elasticity for different level of deformation.

Unlike brains which have clear surfaces that can be modeled with physical structures, lymph node regions do not have surfaces, and usually consist of multiple anatomical entities which make them difficult to deform with physical models. Free-form deformation can be more flexible, as it does not require a segmentation process or any knowledge regarding the physical attributes of the anatomical structures in the regions of interests.

2.4 Image Similarity and 3D Shape Matching

Similarity measurement has been a subject of great interest in research areas such as image database retrieval and medical case base study. Most content-based image retrieval work uses low-level image features like color and texture for image representation to find similar matches between images [53]. Several studies [54] [55] also focus on shape-based indexing and similarity for medical images, which can be more challenging because of the variety and dynamic nature of the anatomical shapes.

With the recent advancement of modeling, scanning and visualizing techniques for 3D shapes, the amount and availability of digital 3D models have been drastically expanded. The subject of matching 3D shapes for content-based 3D shape retrieval has been of interest to many researchers in computer vision and computer graphics. Research groups from Princeton University [59], National Taiwan University [60], and Utrecht University [61] have experimental systems that search similar 3D models of a given target object.

These traditional 3D shape retrieval systems mostly experiment with artificial models such as CAD models, 3D laser scanner output, or partial 3D shape surfaces in VRML. They also mostly focus on classifying 3D models of very different shapes, for example, airplane versus car, or human versus dog. While these experimental systems can match models of the same classes to a certain degree of success, they usually fall short of distinguishing the finer details of objects within a class.

Recent reviews of 3D shape matching techniques were done by Iyer [63] and Tangelder [64]. A majority of the 3D shape matching systems use feature-based

methods, which compare geometric and topological properties of 3D shapes. Methods using features or distributions work reasonably well in classifying objects of different shapes, but they do not discriminate between objects of the same class such as the head and neck anatomy of different patients. The matching process is usually done by computing a distance between feature vectors representing the different objects. Most systems do not give many details on the distance measurements or their comparison methods, although they usually imply a Euclidian vector space model and use either a simple (weighted) Euclidean distance or a city-block (L_1 Minkowski) distance.

In the medical domain, similarity-based retrieval is commonly used by physicians who want to compare imaging studies from a new patient to those from a database of prior patients to help them determine the diagnosis and potential treatment options. Ruiz *et al.* [62][71][72] developed numeric quantitative shape descriptors to characterize skull morphology. These descriptors range from a single number per planar slice to a large matrix of numbers. Lin *et al.* [73] also defined a symbolic shape descriptor for skull images, which is a vector of probabilities obtained from a bag-of-words approach to shape description. These descriptors are derived from CT planar slices defined by internal brain landmarks and are used to find similar craniosynostosis patients for intervention planning. Instead of classifying objects of different shapes, these shape descriptors are designed to discriminate between objects in the same class and to distinguish finer differences between similar shapes.

Chapter 3 Image Registration with Landmark Information

Image registration tools, that align different modalities of images on the same patient, e.g. CT to MR or PET, have been effective in assisting physicians to decide what regions to treat during the course of the clinical radiation therapy, but the actual contours of the Clinical Target Volume (CTV) still have to be drawn manually by the radiation oncologists. By applying image registration methods to align CT images from two different subjects, we hypothesize that a reference model, with images and standard lymph node regions pre-drawn, can be mapped to a target patient to automatically define for that patient the approximate locations of the nodal regions. This is a more challenging problem for image registration, since it involves matching between two different instances of human anatomy, rather than two images of the same anatomy.

Anatomical landmarks are commonly utilized in image registration methods, which use landmark points to match the image properties in different image sets and bring them into alignment. They are also often used in combination with non-rigid elastic or fluid-based image registration methods, for example, Christensen *et al.* [25] use interactive methods to locate anatomical landmarks that define the Frankfort Horizontal Plane, the Median Sagittal Plane, and the Coronal Plane; they then use those planes to estimate the rigid registration before running non-rigid registration with a different method (elastic model). We propose a new method that incorporates landmark correspondence with a non-rigid mutual information image registration method.

3.1 Background

Mattes and Haynor [39] implemented a multi-resolution non-rigid (deformable) image registration method using B-spline image representation and maximization of mutual information. The method was effective in the intra-subject multimodality (PET-CT) lung image registration application, as the deformations between the image sets are limited. Our proposed method is derived from this work and incorporates landmark information to improve the results of inter-subject registration of more complicated anatomy in the head and neck.

3.1.1 Mutual Information

Mutual information is an entropy-based measure of image alignment derived from probabilistic measures of image intensity values [24, 28] and has been used in many intrasubject, multimodal applications.

Definition 1: Two random variables A and B, with marginal probability distributions $p_A(a)$ and $p_B(b)$, and joint probability distribution $p_{AB}(a, b)$, are statistically independent if $p_{AB}(a, b) = p_A(a) \bullet p_B(b)$, while they are maximally dependent if they are related by a one-to-one mapping T: $p_A(a) = p_B(T(a)) = p_{AB}(a, T(a))$. Mutual Information, $I(A, B)$, measures the degree of dependence of A and B by measuring the distance between the joint distribution $p_{AB}(a, b)$ and the distribution associated with the case of complete independence $p_A(a) \bullet p_B(b)$, by means of the Kullback–Leibler measure [74], i.e.,

$$I(A, B) = \sum_{a,b} p_{AB}(a,b) \log \frac{p_{AB}(a,b)}{p_A(a) \bullet p_B(b)} \qquad (1)$$

3.1.2 B-spline Image Representation

Thevenaz and Unser [40] used a B-spline basis to represent the images and model deformations. Mattes and Haynor [36] implemented a B-spline image representation in a multi-resolution optimization approach, to align PET-CT images from the same patient using free-form deformation.

A spline curve is a series of piecewise polynomial segments that are smoothly connected at joining points, called knots. A spline curve of degree *n* has polynomial segments, each of degree *n*, implying the need for *(n+1)* polynomial coefficients to represent each segment. This spline can be uniquely characterized in terms of a B-spline expansion:

$$s(x) = \sum_i c(i)\beta^{(n)}(x-i) \tag{2}$$

where *s(x)* is a spline curve represented by the linear combination of integer-shifted B-splines of order *n*. B-splines, defined below, are symmetrical, bell-shaped functions constructed from the *(n+1)*-fold convolution of a rectangular pulse β^0:

$$\beta^{(0)}(x) = \begin{cases} 1 & -\frac{1}{2} \le x < \frac{1}{2} \\ 0 & \text{otherwise} \end{cases} \tag{3}$$

$$\beta^{(n)}(x) = \underbrace{\beta^{(0)} * \beta^{(0)} * \ldots * \beta^{(0)}}_{(n+1)\text{times}} \tag{4}$$

For example, in the case of *n=3* we have the normalized central cubic B-spline:

$$\beta^{(3)}(x)=\begin{cases}\frac{1}{6}\left(4-6x^2+3|x|^3\right) & 0\le|x|<1\\ \frac{1}{6}\left(8-12|x|+6x^2-|x|^3\right) & 2\le|x|<2\\ 0 & 2\le|x|\end{cases} \tag{5}$$

One other advantage of using B-splines is that they are easy to manipulate. For instance, we can obtain derivatives through the following formula:

$$\frac{d\beta^{(n)}(x)}{dx}=\beta^{(n-1)}(x+\frac{1}{2})-\beta^{(n-1)}(x-\frac{1}{2}) \tag{6}$$

Splines are easy to extend to higher dimensions; for example, the spline model for a particular real-valued location (*x, y, z*) in the image volume is given by

$$f(x,y,z)=\sum_{i=\lfloor x-1\rfloor}^{\lfloor x+2\rfloor}\sum_{j=\lfloor y-1\rfloor}^{\lfloor y+2\rfloor}\sum_{k=\lfloor z-1\rfloor}^{\lfloor z+2\rfloor}c(i,j,k)\beta^{(3)}(x-i)\beta^{(3)}(y-j)\beta^{(3)}(z-k) \tag{7}$$

B-spline bases can be used to represent an image to make it a continuous function $f(\mathbf{x})$ for better interpolation and sampling results. Values of $f(\mathbf{x})$ for non-integer $\mathbf{x}$ can be interpolated with the samples $f_i = f(\mathbf{x}_i)$, $\mathbf{x}_i \in V$ by:

$$f(\mathbf{x}_i)=\sum_i c_i\beta(\mathbf{x}-\mathbf{x}_i) \tag{8}$$

which is a more compact expression of equation (7) by using a vector notation for indexing the summation and subscripting the spline coefficients.

3.1.3 Transformation and Deformation

The transformation of a point $\mathbf{x} = [x, y, z]^T$ in the reference image coordinates to the test image coordinate is defined by a 3×3 homogeneous rotation matrix **R**, a 3-element transformation vector **T** and a deformation term $\mathbf{D}(\mathbf{x}|\boldsymbol{\delta})$:

$$\mathbf{g}(\mathbf{x}|\mu) = \mathbf{R}(\mathbf{x} - \mathbf{x}_C) - \mathbf{T}(\mathbf{x} - \mathbf{x}_C) + \mathbf{D}(\mathbf{x}|\boldsymbol{\delta}) \tag{9}$$

where $\mathbf{x}_C$ is the center of the reference volume. A rigid body transformation defined by **R** and **T** was first calculated, and it was used as the initial transformation for the deformation process. The deformation term $\mathbf{D}(\mathbf{x}|\boldsymbol{\delta})$ gives an x-, y-, and z- offset for each given **x**. Hence the transformation parameter vector $\boldsymbol{\mu}$ becomes

$$\boldsymbol{\mu} = \{\gamma, \theta, \phi, t_x, t_y, t_z; \boldsymbol{\delta}_j\} \tag{10}$$

The first three parameters γ, θ, ϕ, are the roll-pitch-yaw Euler angles of **R**, the rotation matrix can be derived as follows:

$$\mathbf{R} = \begin{bmatrix} \cos\gamma\cos\theta & \cos\gamma\sin\theta\sin\phi - \sin\gamma\cos\phi & \cos\gamma\sin\theta\cos\phi + \sin\gamma\sin\phi \\ \sin\gamma\cos\theta & \sin\gamma\sin\theta\sin\phi + \cos\gamma\cos\phi & \sin\gamma\sin\theta\cos\phi - \cos\gamma\sin\phi \\ -\sin\theta & \cos\theta\sin\phi & \cos\theta\cos\phi \end{bmatrix} \tag{11}$$

The translation vector **T** is defined by $[t_x, t_y, t_z]^T$. **T** and **R** together define the rigid body transformation.

Lastly, $\boldsymbol{\delta}_j$ is the set of the deformation coefficients. The deformation was modeled on cubic B-splines [40] because of their computational efficiency (via separability in multidimensional expression), smoothness, and local control. The

deformation is defined on a sparse, regular grid of control points λ_j, each has an associated x-, y-, and z- components of the deformation. The resolution

$$\rho = [\rho_x, \rho_y, \rho_z] \tag{12}$$

of the deformation determines the spacing of the grid and can be anisotropic. The set of control points is a regular grid with spacings

$$\Delta\rho = [\Delta\rho_x, \Delta\rho_y, \Delta\rho_z]^T = \left[\frac{q_x - 1}{\rho_x - 1}, \frac{q_y - 1}{\rho_y - 1}, \frac{q_z - 1}{\rho_z - 1}\right]^T \tag{13}$$

where q_x, q_y, and q_z are the dimensions of the reference image. Figure 6 shows an example of a control point grid on one axial slice where each of the control points has its own independent x-, y-, and z- components of the deformation.

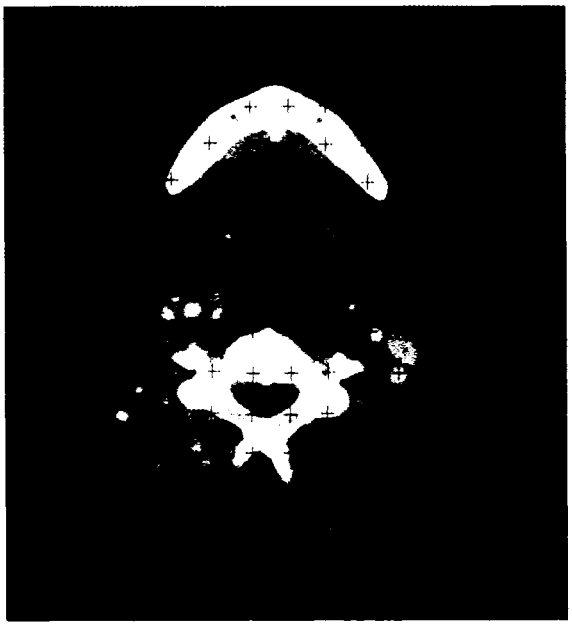

Figure 6: Example of control point grid on an axial slice, ρ_x=15, and ρ_y=15.

The deformation at any point $\mathbf{x} = [x, y, z]^T$ in the reference image is interpolated using a cubic B-spline convolution:

$$\mathbf{D}(\mathbf{x}|\boldsymbol{\delta}) = \sum_j \boldsymbol{\delta}_j \boldsymbol{\beta}^{(3)}\left(\frac{\mathbf{x} - \boldsymbol{\lambda}_j}{\Delta\boldsymbol{\rho}}\right) \tag{14}$$

by moving the control points, intermediate deformation values are computed by cubic spline interpolation between the control points.

3.1.4 Probabilities

The joint probability distribution of the test image (f_T) and the transformed reference image ($f_R \circ \mathbf{g}$) is calculated using the Parzen window density estimation [39] and is given by:

$$p(l, k|\boldsymbol{\mu}) = \alpha \sum_{\mathbf{x}\in V} \gamma\left(k - \frac{f_R(\mathbf{x}) - f_R^0}{\Delta b_R}\right) \times \beta\left(l - \frac{f_T(\mathbf{g}(\mathbf{x}\,|\,\boldsymbol{\mu})) - f_T^0}{\Delta b_T}\right) \tag{15}$$

where α is a normalization factor to ensure $\Sigma p(l, k) = 1$, γ is the zero-ordered spline Parzen window, and β is the cubic spline Parzen window. The image intensity values are normalized by the minimum intensity value, f_R^0 or f_T^0, and the intensity range of the histogram bins, Δb_R or Δb_T.

The marginal probability for the test image p_T is computed from the joint probability distribution equation (15),

$$p_T(l|\boldsymbol{\mu}) = \sum_k p(l, k\,|\,\boldsymbol{\mu}) \tag{16}$$

The marginal probability for the reference image p_R is independent of the transformation parameters, and can be computed as:

$$p_R(k) = \alpha \sum_{\mathbf{x} \in V} \gamma\left(l - \frac{f_R(\mathbf{x}) - f_R^0}{\Delta b_R}\right) \tag{17}$$

The negative of the mutual information between the test and reference images is used as the image discrepancy measure, which can be expressed as a function $S(\boldsymbol{\mu})$ of the transformation parameter vector $\boldsymbol{\mu}$. Using equation (1), we can compute $S(\boldsymbol{\mu})$ with the joint and marginal probabilities of the test image (f_T) and the transformed reference image ($f_R \circ \mathbf{g}$):

$$S(\boldsymbol{\mu}) = -\sum_l \sum_k p(l,k \mid \boldsymbol{\mu}) \log \frac{p(l,k \mid \boldsymbol{\mu})}{p_T(l \mid \boldsymbol{\mu}) p_T(k)} \tag{18}$$

where k, l are the indices of the probability distributions of the reference and test images corresponding to the intensity values.

3.1.5 Algorithm

We adapt the Mattes and Haynor algorithm [36], which was developed for registering one patient's PET and CT data to register CT images of two different persons. To align the patient image with the transformed reference image, we find the set of transformation parameters $\boldsymbol{\mu}$ that maximizes an image similarity function S:

$$\boldsymbol{\mu}_{\text{optimal}} = \text{argmax}_{\boldsymbol{\mu}} S(\boldsymbol{\mu}) \tag{19}$$

The algorithm uses mutual information to measure the similarity (or discrepancy). It is calculated by estimating the marginal and joint probability distribution (histogram) of the intensity values of the test and reference images. Figure 7 shows the flow chart of the registration algorithm.

We use L-BFGS-B [42], a limited-memory, quasi-Newton minimization package, to reduce the cost function $S(\mu)$ in equation (15) until termination criteria are satisfied. The limited-memory method is useful because of the high dimensionality of the parameter space μ in equation (10). L-BFGS-B also provides an additional advantage in that it allows bound constraints on the independent variables; although this is not yet used in previous work, we will try to take advantage of it in the future work.

In order to avoid local minima, and to decrease computation time, we use a hierarchical multi-resolution optimization scheme, as shown in the flow chart. We initially optimize for a gross deformation to the large anatomical features. As we increase the resolution, we deform towards increasingly fine alignments.

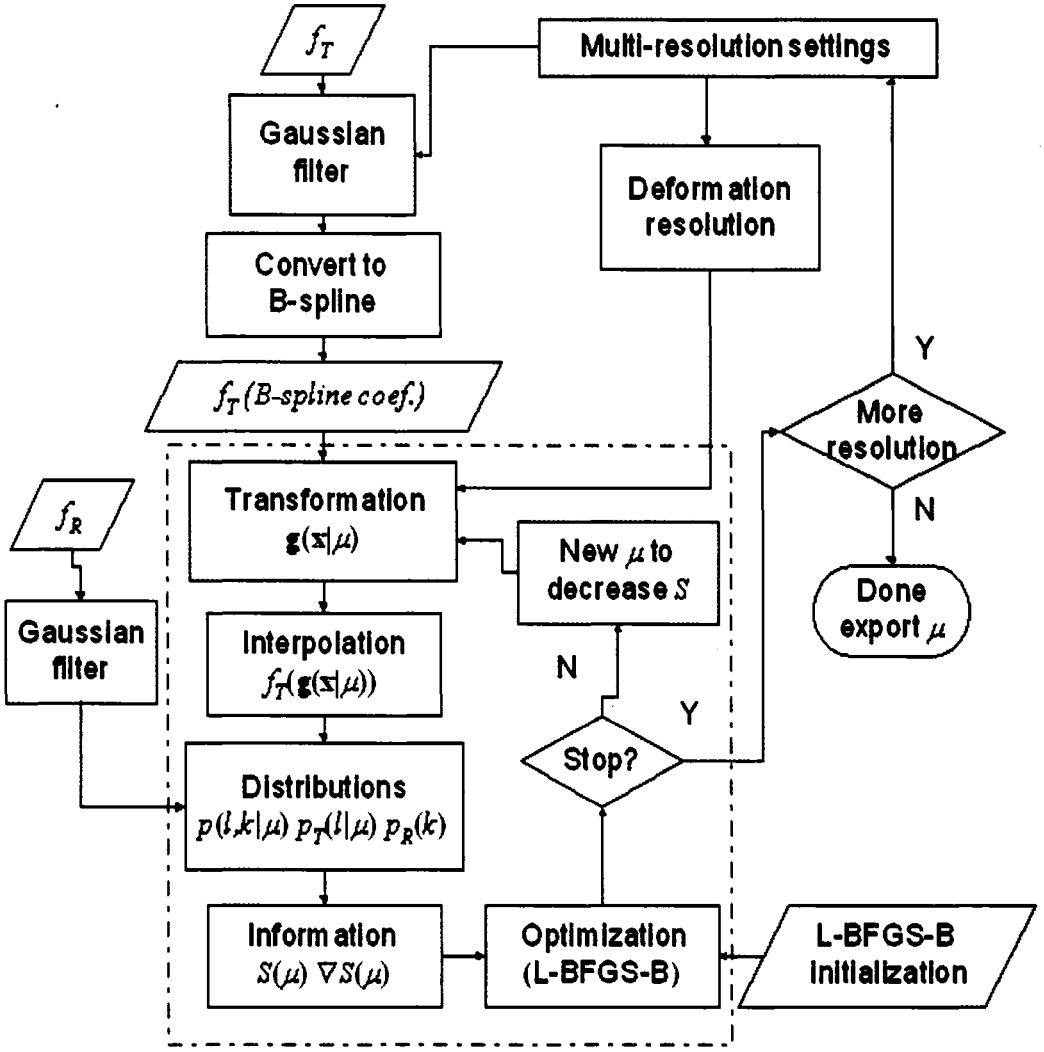

Figure 7: The registration algorithm in a multi-resolution framework. f_T and f_R are the test and reference images respectively. The dash line area is the core for computing and optimizing mutual information for a single resolution step. **x** is any geometric location in the reference image. We start with a set of test points in the reference image space, first calculate the corresponding location in the test image $\mathbf{g}(\mathbf{x}|\mu)$, use B-spline interpolation to calculate the intensity at those location. We can then calculate joint probability $p(l, k|\mu)$, marginal probabilities $p_T(l|\mu)$, $p_R(k)$, and mutual information $S(\mu)$. An optimization function can then be called to find a new set of transformation parameter μ.

3.2 Finding Landmark Correspondences

We choose to use 3D anatomical structure surfaces as landmarks because virtually no 1-D (points) or 2D (lines) anatomical features that can be used as landmarks are defined in the head and neck region. We propose an auto-segmentation method for head and neck CT images that can generate 3D surface meshes for key anatomical structures in the region between the cranial base and the thoracic inlet. The details of this segmentation method will be described in the following chapter. Surface meshes of mandible, hyoid bone, spinal cord, and outer body contour are used as our referenced landmarks because of their proximity to the nodal regions of interest, high contrast, and consistent location, size and shape.

We use Shelton's method [49] to find correspondences between surface meshes. The following energy function for which smaller values indicate better correspondences is defined to evaluate possible correspondence relations:

$$\boldsymbol{E}(\boldsymbol{C}) = \boldsymbol{E}_{\text{sim}}(\boldsymbol{C}) + \alpha \boldsymbol{E}_{\text{str}}(\boldsymbol{C}) + \beta \boldsymbol{E}_{\text{pri}}(\boldsymbol{C}) \tag{20}$$

where **C** is the function that maps points on surface **A** to matching points on surface **B**, α and β are weight parameters, $\boldsymbol{E}_{\text{sim}}$ is the similarity term which measures how closely **C** matches points on **A** to points on **B**, $\boldsymbol{E}_{\text{str}}$ is the structural term that minimize the distortion of surface **A**, and $\boldsymbol{E}_{\text{pri}}$ is the "prior information" term which ensures **C** represent a plausible deformation. Let us define $\boldsymbol{P}_{\mathbf{X}}(q)$ to be the point on the surface **X** closest to the point q. We will then define $\boldsymbol{E}_{\text{sim}}$ as

$$\boldsymbol{E}_{\text{sim}}(\boldsymbol{C}) = \int_{C(A)} \left\| c - P_B(c) \right\|^2 dc + \int_B \left\| b - P_{C(A)}(b) \right\|^2 db \tag{21}$$

This is the sum of the integrals over each surface of the squared distance from points on that surface to the other surface, or the external force that drive the surface warp.

The remaining two terms are the internal forces that maintain the integrity of the shape of the transformed surface. Shelton uses the "directional springs" and "normal springs" to model the internal energy that minimizes the deformation of the surface. For a directional spring connecting the two points p and q, the energy of that spring under the correspondence **C** is

$$\boldsymbol{E}_{\mathrm{ds}}(p, q, \boldsymbol{C}) = \frac{\left\|(p-q)-(C(p)-C(q))\right\|^2}{\left\|p-q\right\|} \tag{22}$$

To create a tight surface and an energy function independent on the parameterization of the surface, we let

$$\boldsymbol{E}_{\mathrm{str}}(\boldsymbol{C}) = \int_A E_{ds}(a, a+da, C) \tag{23}$$

This corresponds to placing direction springs continuously over the entire surface **A**, which ensures the similarity between C(A) and A.

We let $\boldsymbol{E}_{\mathrm{s}}(p, q, \boldsymbol{C})$ be similarly defined for a normal spring of rest length 0,

$$\boldsymbol{E}_{\mathrm{s}}(p, q, \boldsymbol{C}) = \frac{\left\|(C(p)-C(q))\right\|^2}{\left\|p-q\right\|} \tag{24}$$

and, in order to penalize discontinuous surfaces, we define $\boldsymbol{E}_{\mathrm{pri}}$ to be

$$E_{\text{pri}}(C) = \int_A E_s(a, a + da, C). \tag{25}$$

The three terms of $E(C)$ do not play equal roles. The first, E_{sim}, must be zero for C to be a true correspondence. The second, E_{str}, exists to guide and select among C functions which set the first term to zero. The last term, E_{pri}, serves to smooth out any noise which may arise due to inaccurate models or an inability to find the true correspondence; as a prior over surfaces, it models the fact that very unlikely correspondences should be discarded in favor of more likely ones which perhaps do not satisfy the other requirements as well.

Thus, the weighting of the various terms in $E(C)$ will be set as follows: α will be initially large to enforce a good correspondence. Over time, it will be reduced to allow the algorithm to drive E_{sim} to zero. β will be set to a small constant value which is inversely proportional to our confidence in our model and ability to find the correct correspondence.

By minimizing the energy function $E(C)$, we have the correspondence between surfaces of the landmark anatomical structures of the reference and target subjects. Let υ_k be the set of landmark points sampled from the mandible, hyoid and other surface meshes of the reference image set or surface **A**, and ϖ_k be their corresponding locations on surface C(**A**) or the transformed surface which matches the test image set and minimize the energy function. The deformation ζ at those landmark points is simply

$$\zeta_k = \varpi_k - \upsilon_k \tag{26}$$

Figure 8 shows an example of the above landmark surface mesh correspondence. Figure 8A shows the mandible and hyoid mesh of the reference

subject or surface **A**, and figure 8B is the mesh of target subject or surface **B**. Figure 8C is the warped mesh of the reference subject to match target subject mesh or $\boldsymbol{C}(\mathbf{A})$ where function $\boldsymbol{C}$ minimizes the energy function $\boldsymbol{E}(\boldsymbol{C})$ in equation (20), and figure 8D illustrate the landmark deformation vectors ζ from equation (26) in 3D space. Figure 9 shows the same example of correspondence on the 2D axial CT slices of the reference and target subjects.

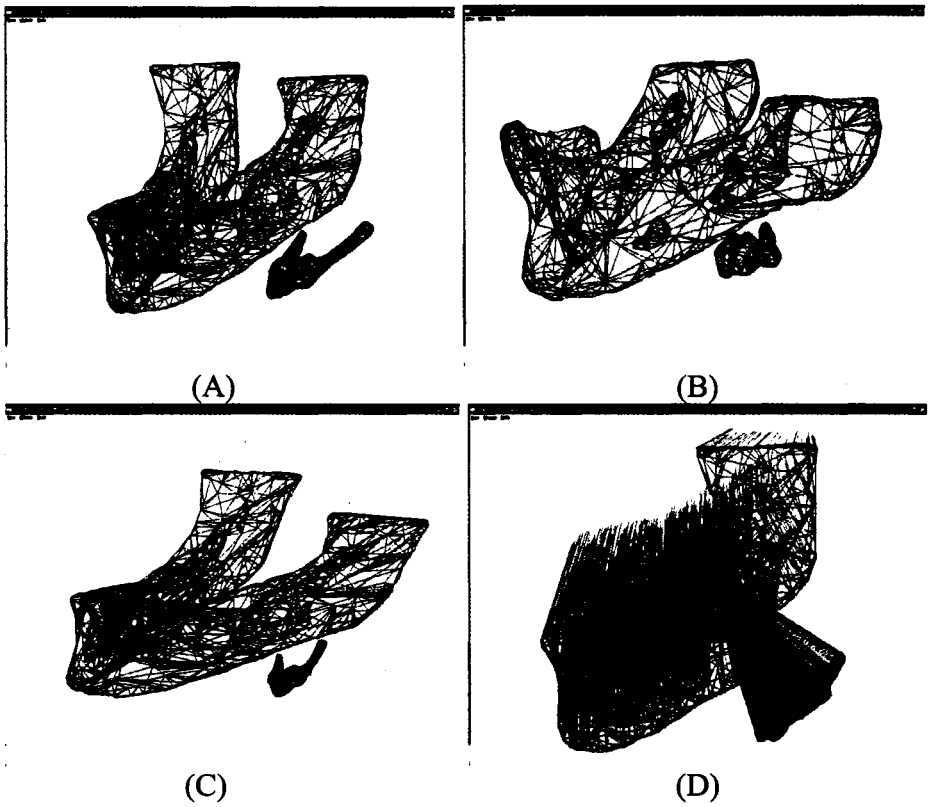

Figure 8: An example of landmark mesh correspondence. (A) shows mandible and hyoid mesh of the reference subject, (B) mesh of target subject, (C) warped mesh of the reference subject to match target subject mesh, and (D) red lines illustrate the deformation vectors ζ from equation (26) in 3D space.

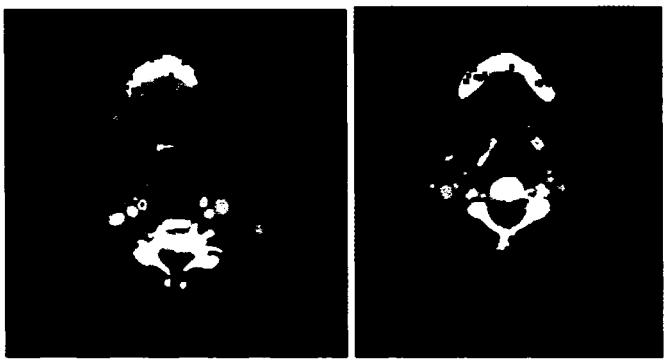

(A) (B)

Figure 9: An example of landmark point correspondence shown on 2D axial CT slices. (A) shows sample landmark points from the 3D mesh of the reference subject, and (B) shows points from the warped mesh of the reference subject to match the target subject mandible and hyoid surfaces.

3.3 Image Registration with Landmark Correspondence

Instead of initializing the deformations at the control points to zero, we propose to use the landmark correspondences to initialize the deformations at the control points at each of the multi-resolution stages. The deformation control points are set to a uniform grid

$$\boldsymbol{\lambda}_j = [l\Delta\rho_x, m\Delta\rho_y, n\Delta\rho_z]^T, \text{ where } 0 \le l \le \rho_x, 0 \le m \le \rho_y, 0 \le n \le \rho_z. \quad (27)$$

and the corresponding deformation values $\mathbf{D}(\boldsymbol{\lambda}_j)$ are either initially set to zero or calculated from the deformation coefficients $\boldsymbol{\delta}_j$ of the previous iteration at a lower resolution of control points as in equation (14).

Then the deformation of each control point that has landmark points in close proximity is modified to the deformation of the closest landmark point as follows

$$D'(\boldsymbol{\lambda}_j) = \begin{cases} \zeta_k & \text{if } \left|\lambda_{jx} - v_{kx}\right| < \frac{1}{2}\Delta\rho_x \;\&\; \left|\lambda_{jy} - v_{ky}\right| < \frac{1}{2}\Delta\rho_y \;\&\; \left|\lambda_{jx} - v_{kx}\right| < \frac{1}{2}\Delta\rho_z \\ D(\boldsymbol{\lambda}_j) & \text{otherwise} \end{cases} \quad (28)$$

where υ_k is the closest landmark point to $\boldsymbol{\lambda}_j$ in the reference image set, and ζ_k is the deformation at υ_k obtained from the surface correspondence in equation (26). A new set of deformation coefficients $\boldsymbol{\delta}$ is then set to the spline coefficients of the new grid of deformation values $\mathbf{D}'(\boldsymbol{\lambda})$ [36]. Finally the transformation parameter vector μ is input to the optimizer for alignment.

Figure 10 shows an example of qualitative comparison of image registration results using the Mattes' method without landmark information and the proposed method which incorporates landmark correspondence. Rows A-E show selected axial CT slices in the neighborhood of the hyoid in various data sets from superior to inferior location. Column 1 shows slices from the reference subject, and column 4 shows slices from the target subject. Columns 2 and 3 show transformed reference images which were re-sampled to match or align with the target images using the transformation function $\mathbf{g}(\mathbf{x}|\mu)$ of equation (9) produced from the image registration procedure. Column 2 is the result of Mattes' image registration method without using landmark information, and column 3 is the result of the proposed method using landmark correspondence. The images in column 3 match better qualitatively to column 4 in several ways. First the outer body contours is closer to the ones of target CT. Second, the superior-inferior location of the hyoid bone and the mandible in column 3 match more closely to the ones in column 4. For example the hyoid bone is in slices (rows) C-E (and beyond) of column 2, but in slices A-D of column 4, and the inferior boundary of the mandible ends in slice D of column 2, but continues beyond slice E in columns 3 and 4. More experiment results will be discussed in Chapter 6, including the quantitative evaluation.

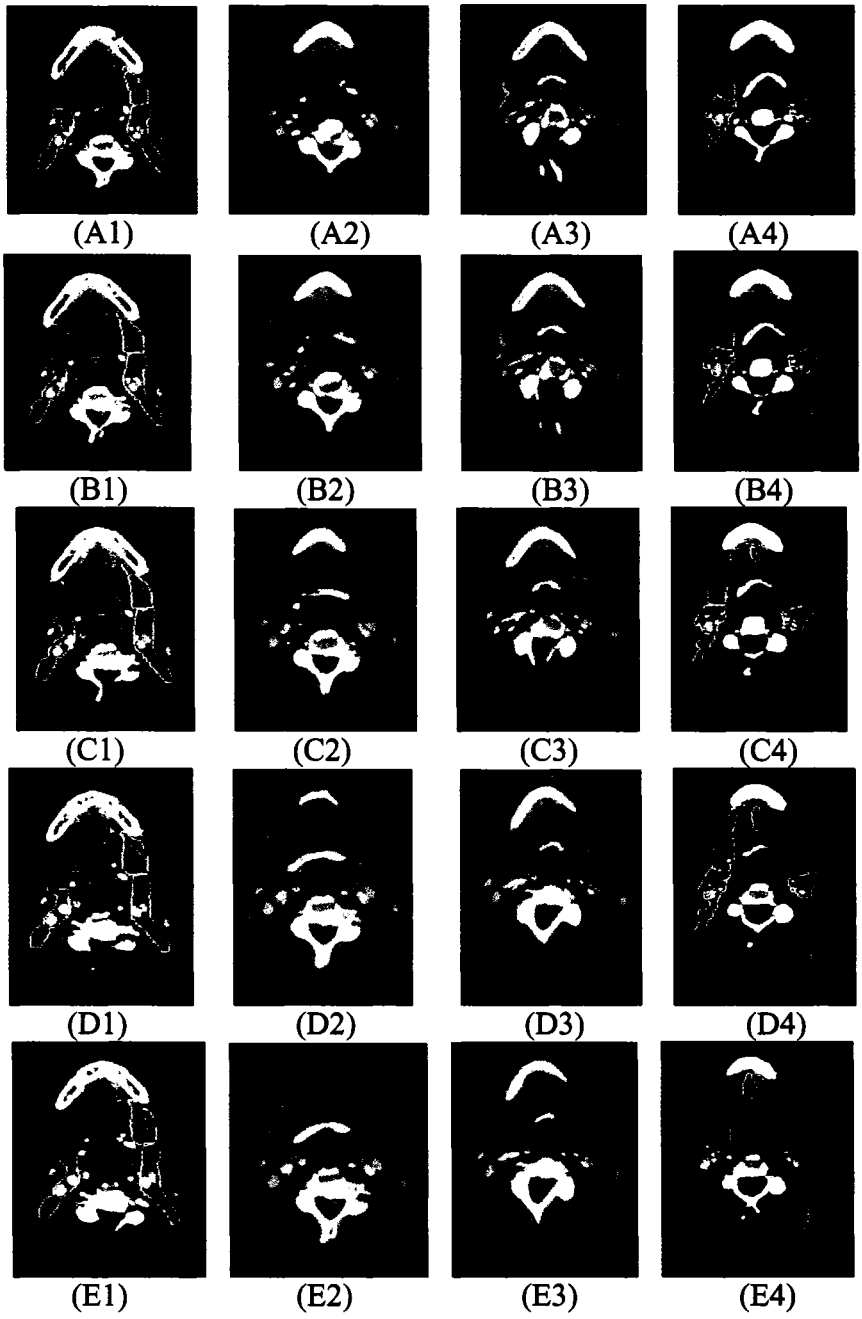

Figure 10: Comparison of results from the image registration methods with and without using landmark correspondence. Rows A-E show selected axial CT slices in the neighborhood of the hyoid in various data sets from superior to inferior. Column 1 shows slices from the reference subject, column 4 from the target subject, column 2 is the result of Mattes' image registration method, and column 3 is the result of the new method using landmark correspondence.

Chapter 4 Auto-segmentation of Head and Neck CT Images

In this era of cross-sectional imaging, it is useful to think of the neck in terms of adjacent anatomical spaces separated by fascial layers extended from the skull base to the thoracic inlet. Although these layers are not usually visible in CT or MR images, their locations can be inferred by knowing their relationships to various anatomical structures that are visible in cross-sectional images. Identifying these anatomical structures in the neck region can facilitate applications such as automated diagnosis by finding abnormality, or computer assisted radiation therapy planning by inferring cervical lymph node regions from these anatomical structures. We propose a system that can automatically segment the neck region from CT images by identifying the cranial and caudal bounding slices and then locating and labeling various anatomical structures in the region.

Fully automatic segmentation in the neck region is particularly difficult, because many soft tissue anatomical entities are small in size and similar in density. Furthermore, they can be directly adjacent to each other or only divided by fascial layers that are not visible in CT images. The relative locations between anatomical entities can vary in different axial locations. Little work has been done specifically for the neck images; one exception is the work of Kruegar *et al* [3] who implemented a semi-automatic system to segment neck CT images for pre-operative planning of neck dissections. We will focus on an automatic segmentation method for radiation therapy patients.

4.1 Background

Kobashi and Shapiro [4] proposed a knowledge-based method to identify anatomical structures that can minimize or eliminate the need for user interaction

using constraint-based dynamic thresholding, negative shape constraints to rule out infeasible segmentation, and progressive landmarking that takes advantage of the different degrees of certainty of successful identification of each structure. Our experimental system is motivated by these techniques.

The drawback of this 2D thresholding approach is the difficulty in determining the optimal threshold, especially in the head and neck region where many structures of similar density are crowded in a tight space. Our proposed method eliminates the need of finding the optimal threshold by combining the 2D thresholding with a 3D active contour procedure. A sub-optimal threshold that only produces partial structure on some axial slices can grow into full 3D volume through 3D active contouring.

3D active contour methods have been widely used for semi-automatic segmentation in medical imaging applications. They usually require user input to "seed" the initial region and/or select the grey scale level range of interests. The 2D regions produced by the knowledge-based dynamic thresholding method can be used as the initial region and eliminate the need of user input.

4.2 Cranial and Caudal Boundary

Williams and Smoker [5, 6] identify the neck in terms of adjacent anatomical spaces separated by fascial layers extended between skull base and thoracic inlet. Physicians often use these two landmarks to determine the range of CT image slices that are of interest for neck surgery or radiation treatment. Our first step is to identify the approximate locations of the skull base and the thoracic inlet in the CT image set.

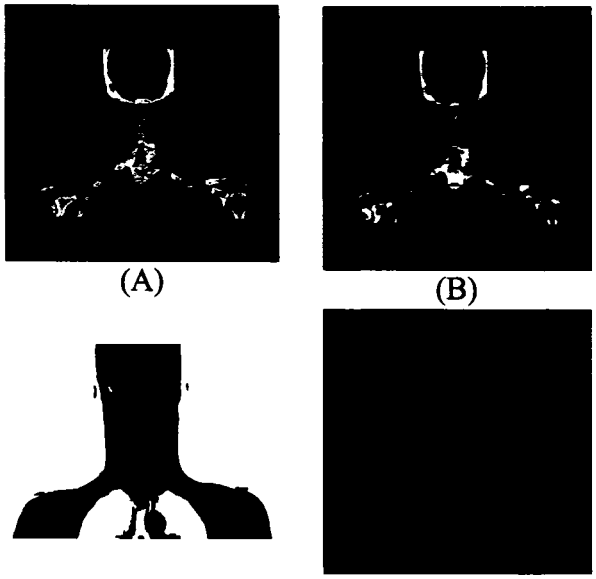

Figure 11: A typical mid-coronal plane of head and neck CT image set, (A) original grayscale, (B) dynamic thresholding result of bone structures, (C) thoracic cavity regions and (D) 3D mesh of thoracic cavity.

While the location of the skull base is not usually clear in the axial CT images, it is more easily identifiable in the coronal view. Figure 11 shows the mid-coronal plane of a typical head and neck CT image set. The skull base can easily be identified by the caudal extremum of the skull region. The thoracic inlet can be approximated by the superior apex of the thoracic cavity.

Identifying proper cranial and caudal boundaries is important as it can be used as references for relative locations for anatomical structures of interest. As we perform inter-subject image registration in a radiation therapy system [10], it is also imperative that each subject has the same region for alignment.

4.3 Segmentation

The proposed system will try to locate the following anatomical structures that can be used as landmarks for lymph node regions in the head and neck, in the following order:

(1) cervical spine,
(2) respiratory tract,
(3) mandible,
(4) hyoid,
(5) thyroid cartilage,
(6) spinal cord,
(7) internal jugular vein,
(8) external jugular vein,
(9) common carotid artery, and
(10) sternocleidomastoid muscle.

This order is defined in accordance with the reliability of successfully detecting the structure. Each structure is associated with domain knowledge including:

(1) Relevant gray tone range, containing the threshold that should segment the structure correctly,
(2) Location relative to the cranial and caudal boundary and overall outer body contour extent described as a normalized range between [0, 1] in the axial, coronal, and sagittal directions.
(3) Location relative to other structures that can be found prior to this structure,
(4) Size in terms of area and extent,
(5) Shape constraints.

The following shows an example of the domain knowledge associated with the hyoid:

```
{
    Hyoid,          // ANATOMY_LABEL label;
    100,            // int i2DAreaMin;
    500,            // int i2DAreaMax;
    1.5,            // float fMaxZExt;
    0.0,            // float fCircularityMin;
    1.0e10,         // float fCircularityMax;
    0,              // float fAspectRatio;
    4095,           // int iThreshHighMax;
    4095,           // int iThreshHighMin;
    1200,           // int iThreshLowMax;
    1180,           // int iThreshLowMin;
    0.4,            // float fBBHigh;
    0.7,            // float fBBLow;
    0.0,            // float fBBFront;
    0.5,            // float fBBBack;
    0.2,            // float fBBLeft;
    0.8,            // float fBBRight;
    KBEF_OPENCLOSE // DWORD dwFlags;
}
```

Segmenting soft tissues in the neck is in general very difficult because adjacent structures can be similar in gray tone with almost no distinct separation between them. We currently focus on the sternocleidomastoid muscle, since it is the most prominent muscle in the neck. While part of the sternocleidomastoid muscle has distinct edges, it can be problematic as the sternal head comes into contact with other muscles and tissues and becomes difficult to separate.

We combine 2D segmentation and 3D active contouring for each anatomical structure we want to identify. For each structure, we first run the dynamic thresholding process to find 2D regions in axial slices according to domain knowledge. Then we run the 3D intensity based region competition active contour method (by ITK, www.itk.org) to build the 3D model using those 2D regions as the seed. This two step process is then repeated for the next structure.

4.4 Algorithm

The dynamic thresholding algorithm adapted from [4] is as follows. For each structure, the system iterates through a range of axial CT slices relative to the cranial and caudal boundaries according to the domain knowledge. The system first sets the initial threshold to the high end of the relevant gray tone range and performs a thresholding operation, morphological operations, and a connected components operation. It will check if there is any region that satisfies the constraints. Candidate regions that overlap with other known structures are excluded. If multiple regions satisfy all the constraints, we choose the one with most overlap with the resulting region of the previous axial slice, or the region with largest area. The threshold is then reduced by a single step (value 5 is currently used,) and the same procedure is repeated. This process continues until the low end of the relevant gray tone range or candidate regions are successfully found. Figure 12 shows contours of structures extracted by the dynamic thresholding process at various axial locations in five different sets of patient CT images. Upon exiting this loop of repeated thresholding, if candidate regions are successfully found, we will go to the 3D active contour process. Figure 14 shows the flowchart of this two-step knowledge-based automatic segmentation algorithm. The 2D dynamic thresholding loop is shown on the right. The 3D active contouring process shown on the lower left will take place if the 2D loop exits successfully.

Since some axial slices may yield successful 2D segmentation results and others do not, we use 3D active contouring to build 3D models from the partial segmentation results. Those 2D regions are used to seed the initial model. The final threshold values for each anatomical entity from the dynamic thresholding process are used to preprocess the raw CT images and isolate the intensity ranges of interest for the active contouring process.

This two step process is repeated for each of the anatomical structures we want to find according the predefined order. Figure 15 shows an example of step by step results of this iterative process. Images A – B shows results for cervical spine segmentation, C – D for mandible, E – F for hyoid, G – H for jugular veins, I – J for carotid arteries, and K – L for sternocleidomastoid muscles. The left column shows the results of dynamic thresholding, where not all axial slices have successfully segmented 2D region. The right column shows the corresponding results of 3D active contouring using results from the left column as seeds.

Figure 16 shows a screen shot of the 3D active contour component. More details of the segmentation tool will be covered in Chapter 6, along with the quantitative evaluation of the result.

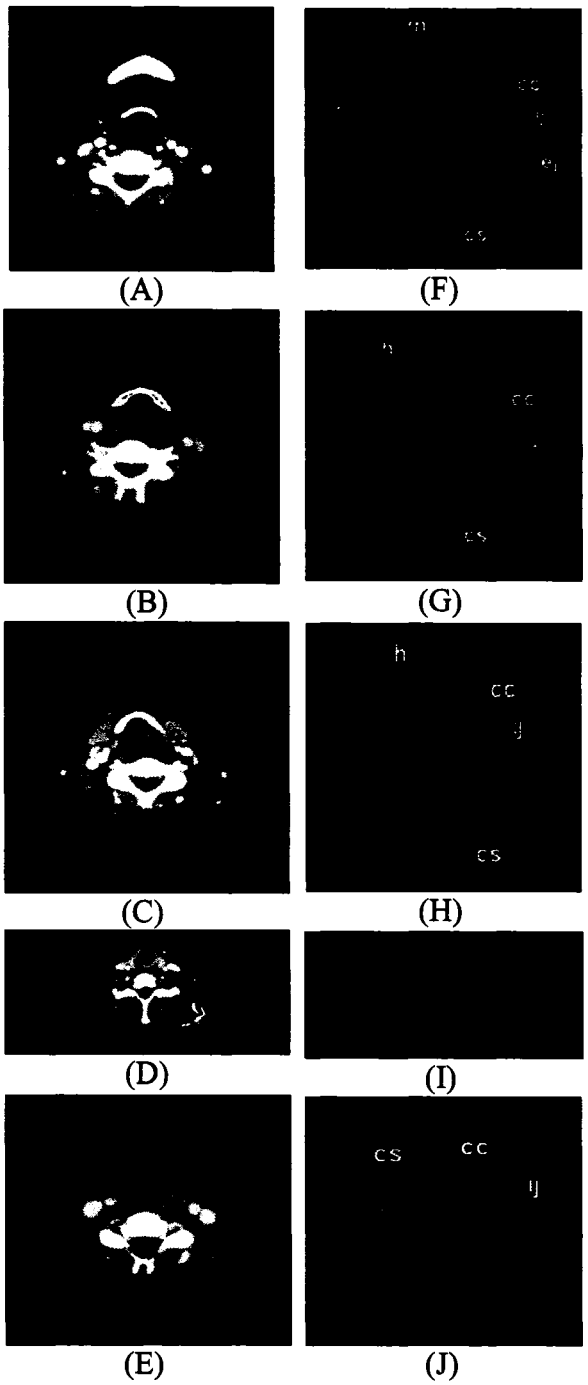

Figure 12: Result samples of dynamic thresholding for bone structures and blood vessels, cervical spine (*cs*), mandible (*m*), hyoid (*h*), common carotid artery (*cc*), internal jugular vein (*ij*), and external jugular vein (*ej*). (A) - (E) are selected sample CT slices from different patients at various axial locations, (F) – (J) are corresponding dynamic thresholding results.

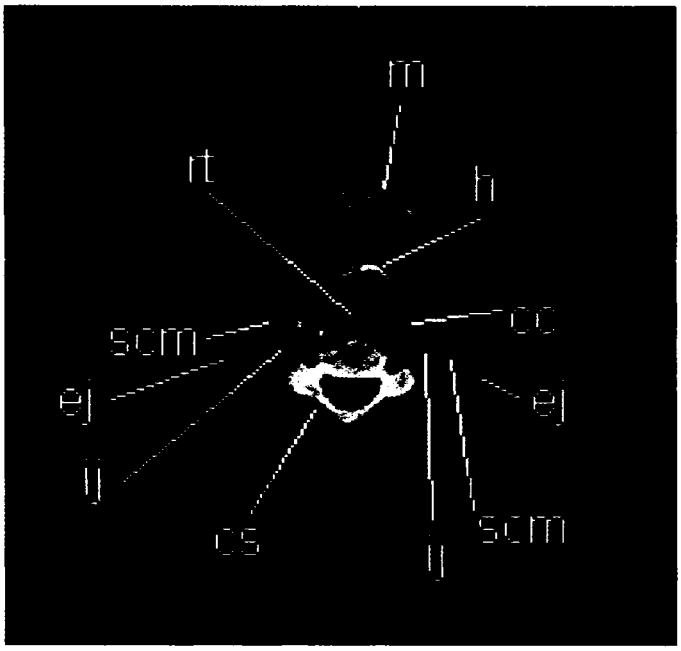

Figure 13: Sample result of automatic segmentation with color label of the following structures, cervical spine (*cs*), mandible (*m*), hyoid (*h*), common carotid artery (*cc*), internal jugular vein (*ij*), sternocleidomastoid muscles (*scm*), respiratory tract (rt), and external jugular vein (*ej*).

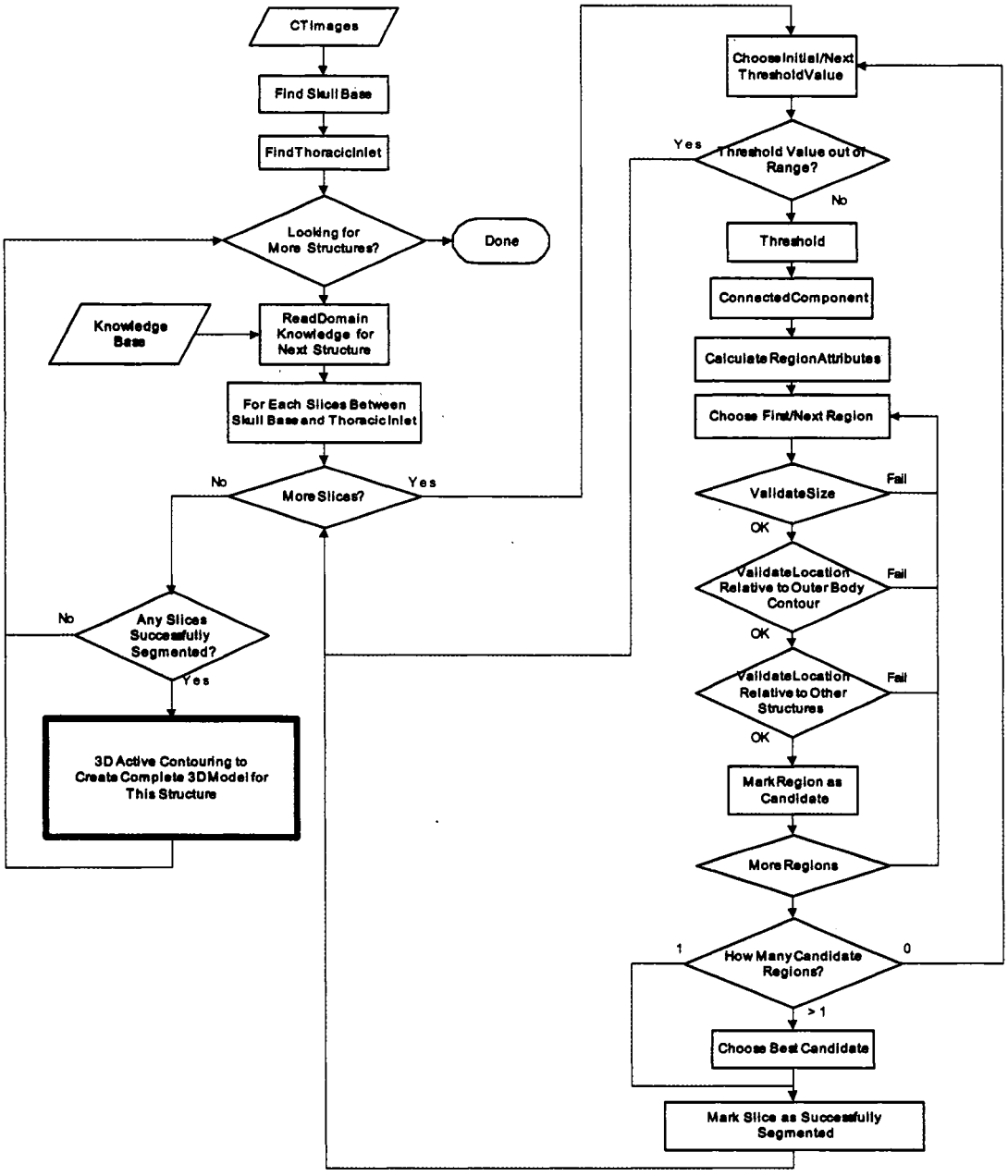

Figure 14: Flowchart of the two step knowledge based automatic segmentation algorithm.

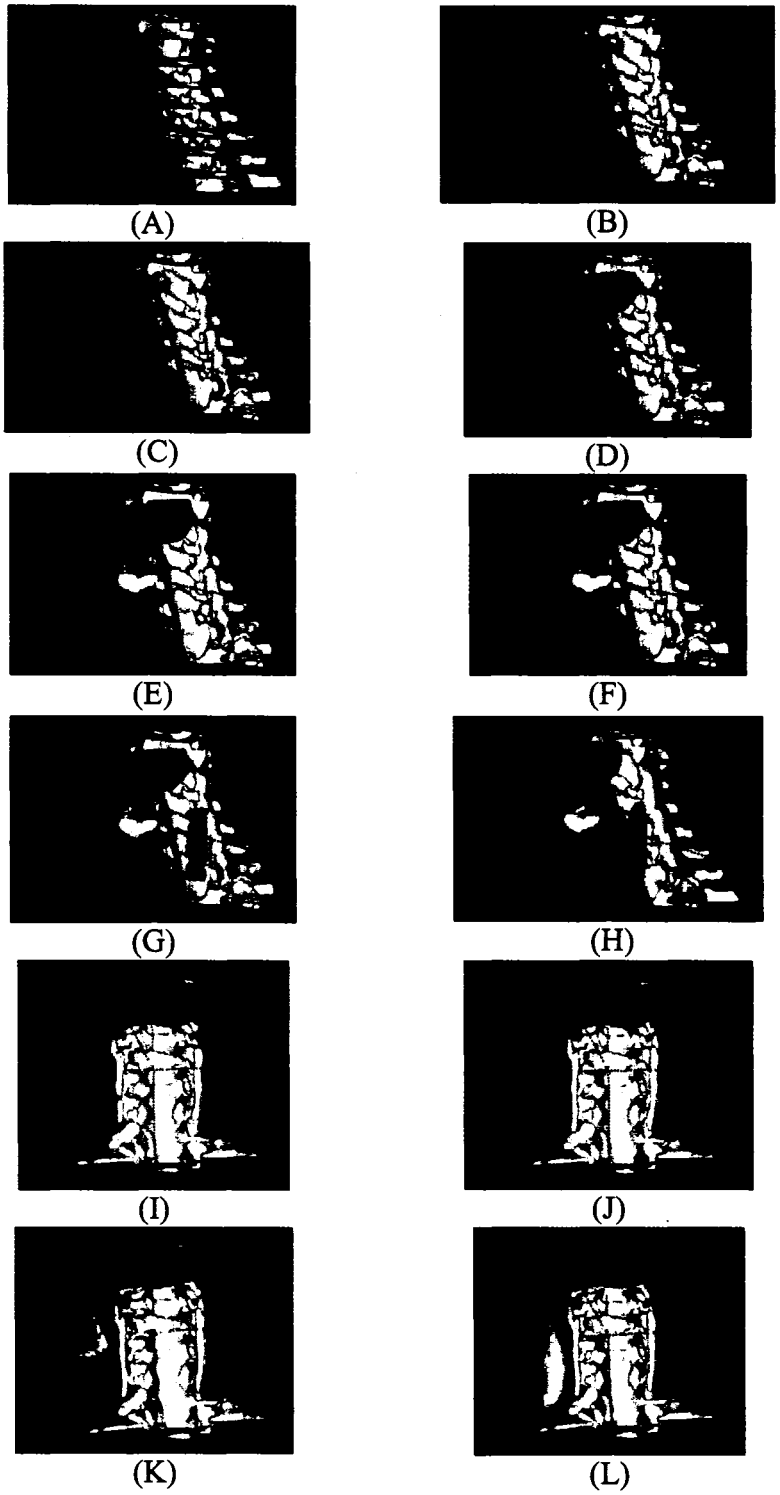

Figure 15: Example of step by step results, left column shows dynamic thresholding results, right column shows 3D active contour results.

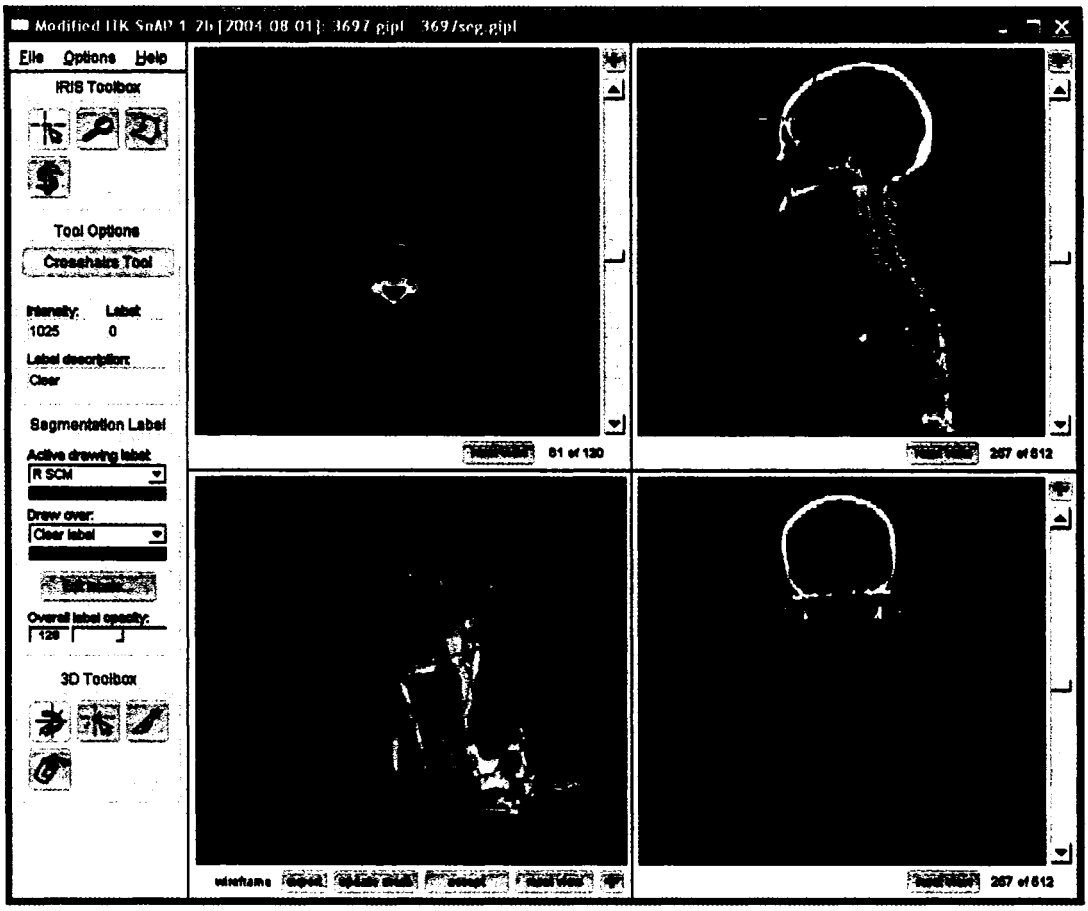

Figure 16: 3D models of the anatomical structures using 2D segmentation results and 3D active contouring.

Chapter 5 Similarity Measurement Based on Anatomical Structural Geometry

Traditional 3D shape retrieval systems [59, 60, 61] mostly experiment with artificial models and focus mainly on classifying 3D models of very different shapes. While these experimental systems can match models of the same classes to a certain degree of success, they usually fall short of distinguishing the finer details of objects within a class.

As we develop a radiation treatment planning system for head and neck cancer patients [57][58], there is an increasing need to identify similar patients whose anatomical structures share similar properties or features. By finding previously treated patients or canonical models with the most similar anatomy in the head and neck region, our system can generate possible lymph node regions for a target patient based on known regions defined in similar patients. We can in turn expedite the radiation treatment planning process, which currently depends on oncologists manually delineating lymph node regions for each patient slice by slice on their CT scans.

Using 3D medical images to find similarity among a known set of patients is becoming a research subject of interest in many medical domains. Ruiz *et al.* [62] use a shape-based similarity measure to find similar craniosynostosis patients for intervention planning. We are proposing a method to find similar head and neck cancer patients for radiation planning. The similarity of head and neck anatomy between patients is based not only on shape features of structures, such as outer body volume, mandible, and hyoid, but also on their relative locations. These types of medical-image-based problems are very domain specific, and are not solved by the traditional shape-based retrieval system. This chapter proposes a fast and

effective way to find similar head and neck patients for the purpose of radiation treatment planning.

5.1 Background

Recent reviews of 3D shape matching techniques were done by Iyer [63] and Tangelder [64]. A majority of the 3D shape matching systems use feature-based methods, which compare geometric and topological properties of 3D shapes. Methods using features or distributions work reasonably well in classifying objects of different shapes, but they do not discriminate between objects of the same class such as the head and neck anatomy of different patients. The matching process is usually done by computing a distance between feature vectors representing the different objects. Most systems do not give many details on the distance measurements or their comparison methods, although they usually imply a Euclidian vector space model and use either a simple (weighted) Euclidean distance or a city-block (L_1 Minkowski) distance.

As we need to compare similarity between anatomical structures from different patients, we do so by measuring the errors between structure surfaces using the 3D Hausdorff distance [47]. Given two aligned surface meshes, S_R and S_T, the distance between a point p_R belonging to S_R and the mesh S_T can be defined as follows:

$$d(p_R, S_T) = \min_{p \in S_T} \| p_R - p \|. \tag{29}$$

We first align meshes S_R and S_T with the Iterative Closest Point (ICP) rigid body registration [65]. Given the 3D point sets $P_R = \{p_i\}$ containing the n vertices of S_R,

the registration process will produce a transformation matrix $\boldsymbol{T}$ which minimize the function

$$D(S_R, S_T) = \sum_{i=1}^{n} d(Tp_i, S_T). \tag{30}$$

The transformed reference mesh $\boldsymbol{TS_R}$ consists of vertices $\{\boldsymbol{Tp_i}\}$, and the Hausdorff distance between $\boldsymbol{TS_R}$ and S_T is given by

$$d_h(TS_R, S_T) = \max_{p \in S_R} d(Tp, S_T). \tag{31}$$

5.2 Feature Extraction

Image-based classification of head and neck lymph node regions has been proposed [2] to provide a more consistently reproducible nodal staging model for cancer patients. We use easily identifiable structures, including the mandible, hyoid, jugular veins and the outer body contour that are relevant to the boundary for the lymph node regions to rapidly produce a distance metric between a query $\boldsymbol{Q}$ and each $\boldsymbol{d}$ in $\boldsymbol{DB}$. The feature vectors that we use to compare two CT scans include three kinds of features: 1) simple numeric 3D regional properties of these structures, such as volume and extents, 2) vector properties or the relative location between structures and 3) shape properties or the surface meshes of these structures. The feature vector consists of the following properties,

- volume and extents of the overall head and neck region,
- surface meshes of the mandible and outer body contour,
- 3D centroid difference vector between mandible and hyoid,
- 2D centroid difference vectors between hyoid and jugular veins, and between hyoid and spinal cord on the axial slice at the centroid of the hyoid,
- normalized centroid locations of the hyoid and the mandible within the region.

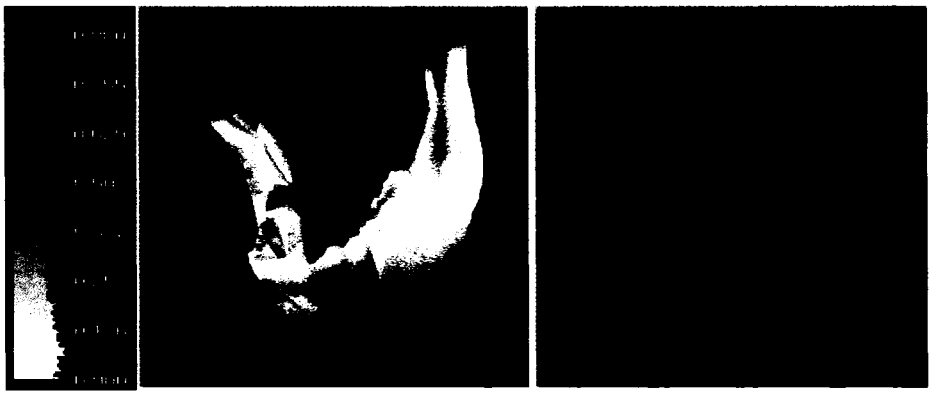

Figure 17: Measuring distance $d(p_R, S_T)$ in between sample point p_R on reference mesh surface on the left and target mesh S_T on the right. The bar graph on the left indicates distance measurement in centimeter corresponding to the shade of S_R.

Given feature vectors F_d and F_Q for model $\boldsymbol{d}$ and query $\boldsymbol{Q}$ in the feature vector space R^N, the following weighed Euclidean distance is used as the distance measure:

$$D_F(F_d, F_Q) = \left[\sum_{i=1}^{N} w_i d_i (F_{d_i}, F_{Q_i})^2 \right]^{\frac{1}{2}} \tag{32}$$

where w_i is the weight parameter, d_i is the distance function for feature i,

$$d_i(f_1, f_2) = \begin{cases} d_h(Tf_1, f_2) & \textit{for mesh features} \\ |f_1 - f_2| & \textit{otherwise} \end{cases} \tag{33}$$

d_h is the Hausdorff distance defined in equation (25), and $\boldsymbol{T}$ is the ICP registration transformation matrix.

The distance between mandible meshes of two subjects is one major discriminating feature of the proposed distance measure. Figure 17 shows the measurement of point to surface distance d as in Equation (29), from which the directional Hausdorff distance d_h between the reference mandible surface mesh to

the target mesh is derived. The mesh on the left with shading indicates the distance from a given point on the surface to the mesh on the right.

5.3 Evaluation

In order to evaluate the proposed distance measure, we ran a set of experiments comparing the results of image registration and the proposed distance measure. All the images used in the experiments are CT scans of head and neck cancer patients performed at the University of Washington Medical Center using a General Electric CT scanner. Thirty five sets of head and neck CT images were selected for the experiment in which all of the slices are 512×512 pixels in axial dimension; the distance between slices varies between 1.25 mm and 3.75 mm for each image set. A 3D deformable image registration process was run on a subset of images to generate lymph node region prediction, which was evaluated quantitatively using the Hausdorff distance. Figure 18 shows the correlation between the proposed distance measure and the result of the 3D deformable image registration between selected patients. The vertical axis shows the Hausdorff distance between the transformed 3D mesh of the reference model lymph nodal region and the corresponding mesh of the test model using the transformation produced by the 3D deformable image registration. The horizontal axis represents the distance measurement, or the weighed Euclidian distance between the test and reference model properties in the feature vector space. Figure 18A compares this to results of lymph node region 1B of the right side, and figure 4B compares it to lymph node region 2. The ideal result should demonstrate strict proportionality between x and y, where smaller distance between feature vectors indicates similar anatomy which should yield better alignment with image registration and smaller Hausdorff distance between the projected and expert-drawn lymph node regions. While most data points in Figure 18 approximate x-y proportionality, a few of them

are outliers. This is mainly due to inconsistent lymph node region contours drawn by various radiation oncologist experts who are influenced by their clinical judgment, rather than purely following the image based classification. These results show promise for further investigation with a larger data set.

The experiments were performed on a Windows PC with Pentium 4 processor and 1GB of memory. The average time taken to calculate a distance measure between feature vectors of two models is approximately 3 seconds, including the ICP rigid body transformation and Hausdorff distance calculation between reference and target meshes. The mutual information based 3D deformable image registration process takes over 20 minutes on average to register two sets of head and neck CT images. As we collect more data and increase the number of reference models, it becomes important to have a fast and effective method to select candidate reference models that can produce the best result. More case by case quantitative analysis will be discussed in Chapter 6.

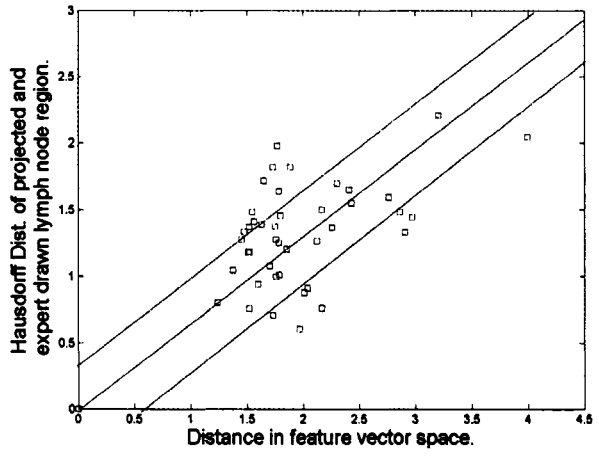

(A)

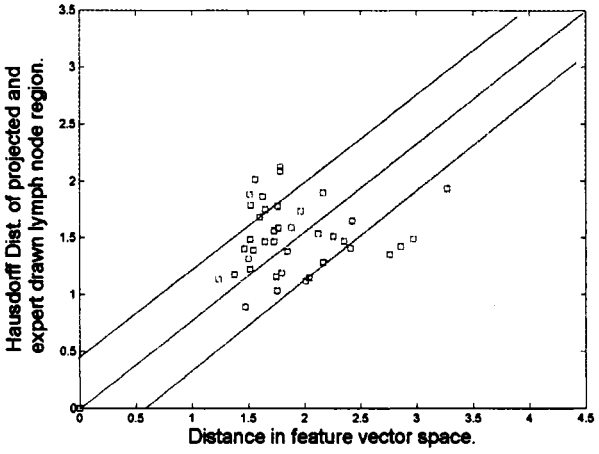

(B)

Figure 18: Comparison of the proposed distance measure (horizontal axis) to the Hausdorff distance between the projected lymph node regions resulting from registration and those hand-drawn by experts (vertical axis): (A) lymph node region 1B right, (B) region 2B right.

Chapter 6 Experiments and Results

In this chapter we report on the experiments with the automatic segmentation and image registration methods. All experiments were run on a personal computer with Microsoft Windows XP © operating system, and all software tools were written in C++, built with Microsoft Visual C++.

6.1 Data Acquisition

CT images are acquired from the PRISM radiation therapy treatment planning system. Head and neck cancer patients who did not have large scale surgical resection are the primary candidates.[1] All the images used in the experiments are CT scans performed at the University of Washington Medical Center using a General Electric CT scanner. Forty six sets of head and neck CT images were selected in which all of the slices are 512×512 pixels in axial dimension; the distance between slices varies between 1.25 mm and 3.75 mm for each image set. A simple automated segmentation pre-process removes the bed and immobilization devices on each CT images. Figure 19 shows a screen shot of the PRISM system, and Figure 20 shows a comparison of a raw and pre-processed CT slice.

[1] The use of CT images is covered by the Human Subject Application #06-3423-E/C 01.

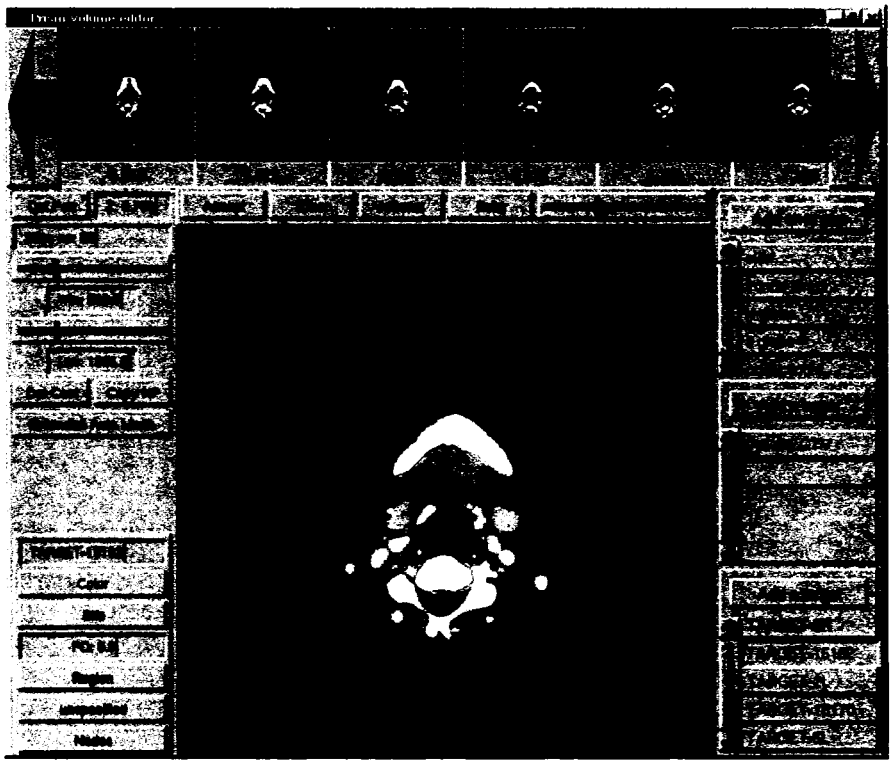

Figure 19: PRISM radiation treatment planning tool.

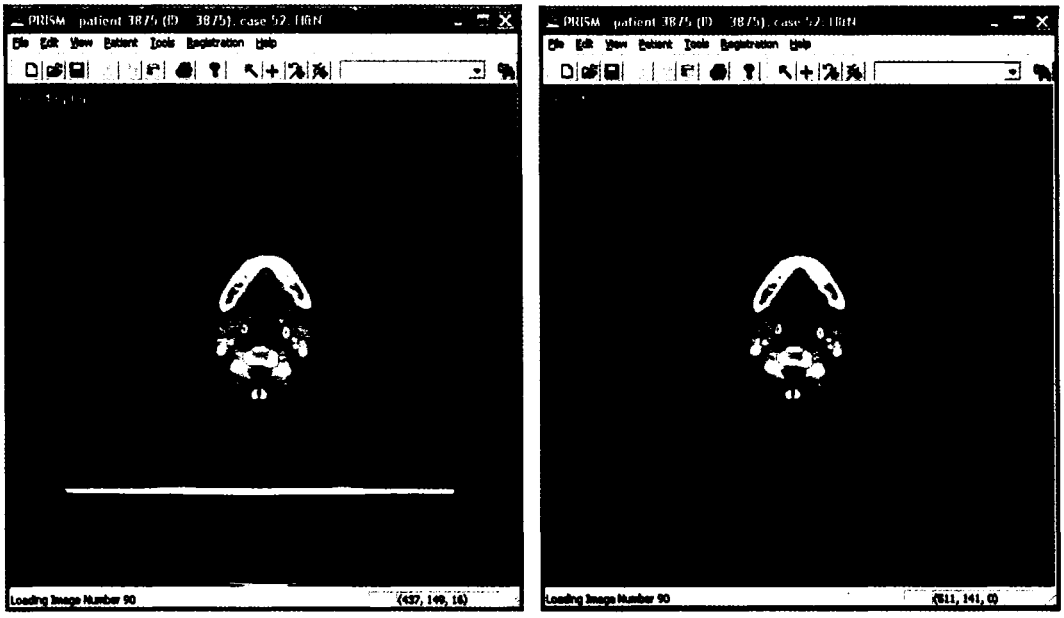

Figure 20: Raw CT and pre-processed images.

6.2 Segmentation Tool

The segmentation procedure identifies the 3D volumes for the anatomical structure of interest, which in turn produces two types of information:
(1) 3D meshes representing the volumes,
(2) 3D geometric properties of the volumes.
We utilize the NLM Insight Segmentation and Registration Toolkit (ITK, www.itk.org) and the Visualization Toolkit (VTK, www.vtk.org) to build our software tools. Commonly used standard data formats are used to store 3D data; GIPL (Guys Image Processing Lab) format [68] is used for 3D grey scale CT image stack and 3D segmentation label files, VTK format is used for 3D meshes. Figure 22 shows the flowchart of the process that produces the meshes and other properties. Figure 23 shows a sample mandible surface mesh generated from the procedure. A label description file defines the anatomical structures and their visual information; an example is shown in Figure 24.

The auto segmentation procedure produces sets of anatomical structure surface meshes that are stored and associated with each subject. Figures 25 and 26 exhibits selected segmentation results in 3D color labeled surface meshes. The success/failure ratio of the segmentation procedure varies depending on the structures. Table 2 and Figure 21 show the success/failure statistic of each structure. The reasons for failure also vary depending on the structures. Segmentation failures are commonly caused by surgical resection in post operative subjects. In addition, thyroid cartilage can fail if the CT resolution is low, i.e. slices are too far apart. Internal jugular veins can fail if it is inseparable from the adjacent muscle or carotid artery. The segmentation procedure is designed with strict rules so that it fails if target structures can not be found, instead of having incorrect result. Few incorrect results are produced in the experiment, with the exception that the carotid artery

can be mistakenly identified as the internal jugular vein if they are clustered together.

Table 2: Auto segmentation success/failure statistics for various anatomical structures.

	Successs	Fail	Incorrect	% of success
Cervical Spine	34	0	0	100.00%
Respiratory Tract	34	0	0	100.00%
Mandible	34	0	0	100.00%
Hyoid	34	0	0	100.00%
ThyroidCartilage	33	0	1	97.06%
Left Internal Jugular Vein	27	3	4	79.41%
Right Internal Jugular Vein	31	1	2	91.18%
Left Carotid Artery	25	9	0	73.53%
Right Carotid Artery	30	4	0	88.24%
Left SCM	24	10	0	70.59%
Right SCM	25	9	0	73.53%
Left External Jugular	6	28	0	17.65%
Right External Jugular	6	28	0	17.65%

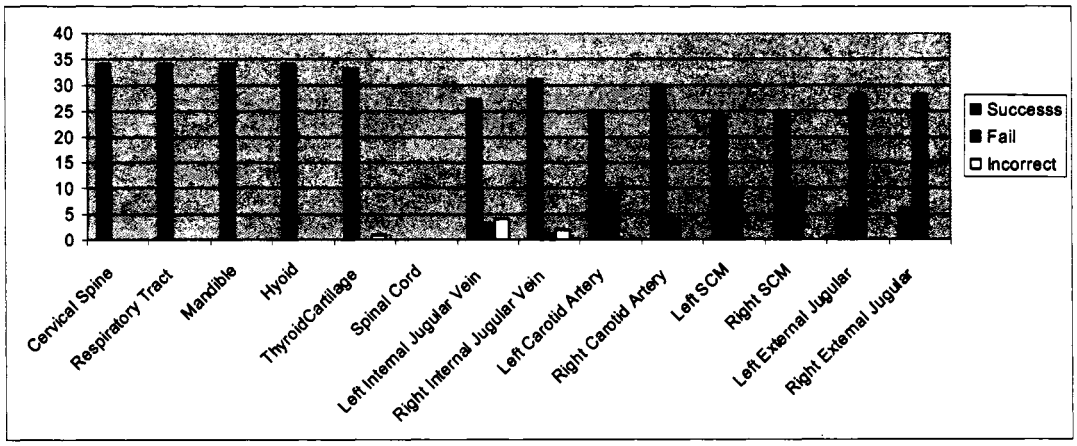

Figure 21: Auto segmentation success/failure statistics for various anatomical structures.

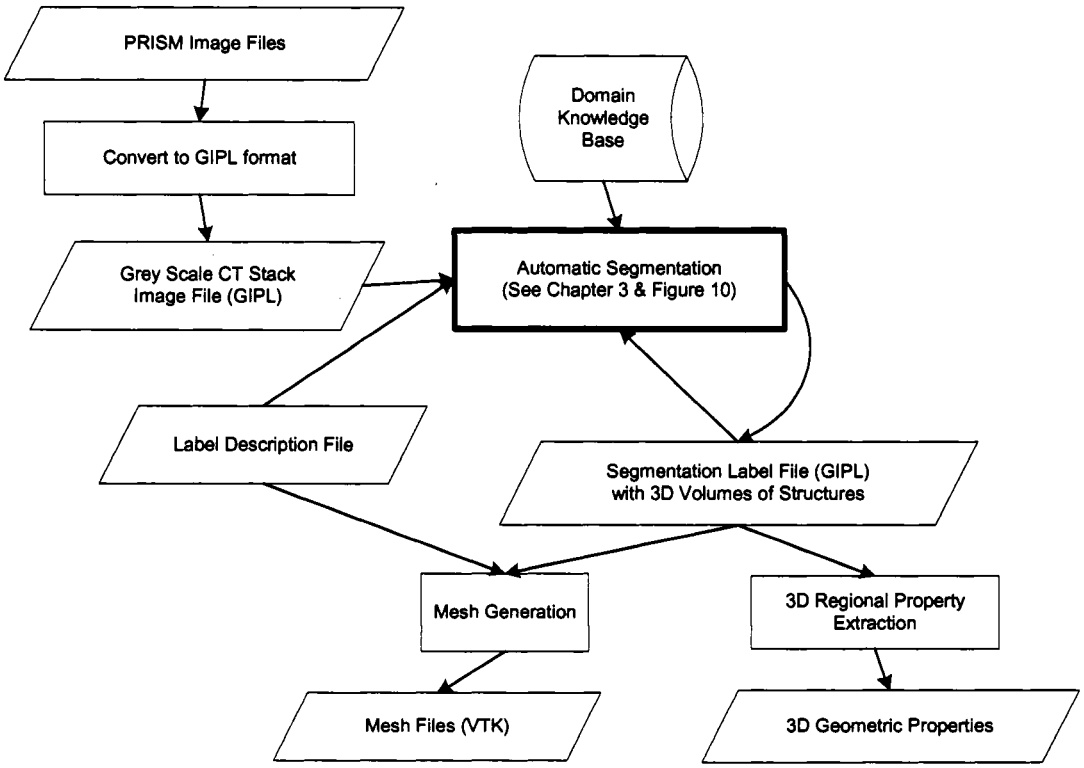

Figure 22: Overall flowchart of the segmentation data generation process.

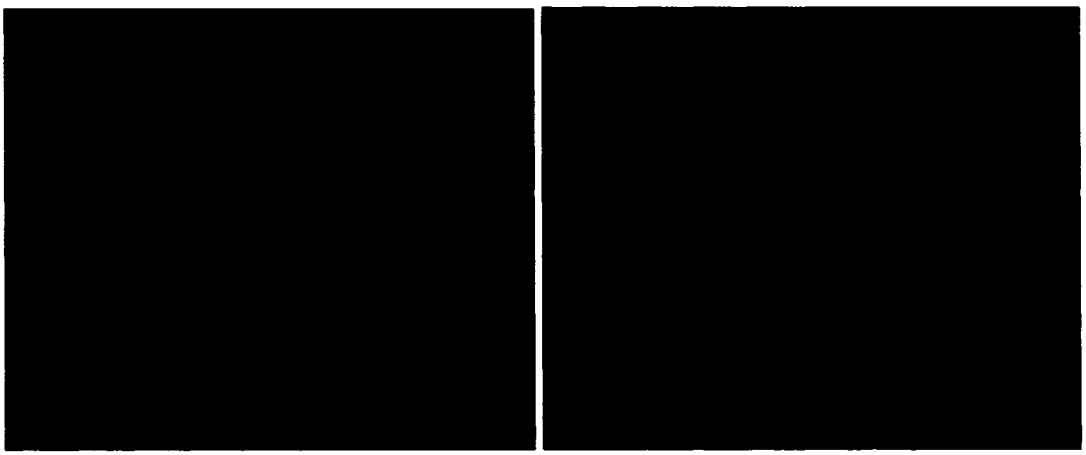

Figure 23: Sample mesh generated from segmentation process, wireframe shown in right.

```
################################################
# Label Description File
# File format:
# IDX   -R-  -G-  -B-  -A--  VIS MSH  LABEL
# Fields:
#    IDX:   Zero-based index
#    -R-:   Red color component (0..255)
#    -G-:   Green color component (0..255)
#    -B-:   Blue color component (0..255)
#    -A-:   Label transparency (0.00 .. 1.00)
#    VIS:   Label visibility (0 or 1)
#    IDX:   Label mesh visibility (0 or 1)
#  LABEL:   Label description
################################################
0     0    0    0        0  0  0    "Clear"
1   255  160  108        1  1  1    "L SCM"
2     0  255    0        1  1  1    "R SCM"
3   163  198  255        1  1  1    "C Spine"
4   255  255    0        1  1  1    "Hyoid"
5     0  255  255        1  1  1    "Mandible"
6   255    0  255        1  1  1    "L Internal Jugular Vein"
7   255    0  255        1  1  1    "R Internal Jugular Vein"
8   255  181    0        1  1  1    "R Common Carotid Artery"
9   255  181    0        1  1  1    "L Common Carotid Artery"
0   181    0    0        1  1  1    "Skull"
11    0    0  181        1  1  1     "Body"
12  132  181   42        1  1  1     "Respiratory Tract"
13   12  181  104        1  1  1     "Thyroid Cartilage"
14  134   87  181        1  1  1     "Cricoid Cartilage"
15    0  128    0        1  1  1     "Cord"
16    0  128  255        1  1  1     "L External Jugular Vein"
17    0  128  255        1  1  1     "R External Jugular Vein"
90  255    0    0      0.5  1  0     "Noise"
98  255    0    0      0.5  1  0     "Bed and Devices"
99  255    0    0      0.5  1  0     "Seperator"
110  155  255   56     0.75  1  1     "Node 1A"
111   20  255  187     0.75  1  1     "Node 1B Right"
112  255  108  105     0.75  1  1     "Node 1B Left"
121   14   65  255     0.75  1  1     "Node 2 Right"
122  124  106  255     0.75  1  1     "Node 2 Left"
131  237  255    0     0.75  1  1     "Node 3 Right"
132  255  247  110     0.75  1  1     "Node 3 Left"
141  255   87  162     0.75  1  1     "Node 4 Right"
142  255   25  235     0.75  1  1     "Node 4 Left"
151  255   95    0     0.75  1  1     "Node 5 Right"
152  255  121   13     0.75  1  1     "Node 5 Left"
```

Figure 24: Label description file.

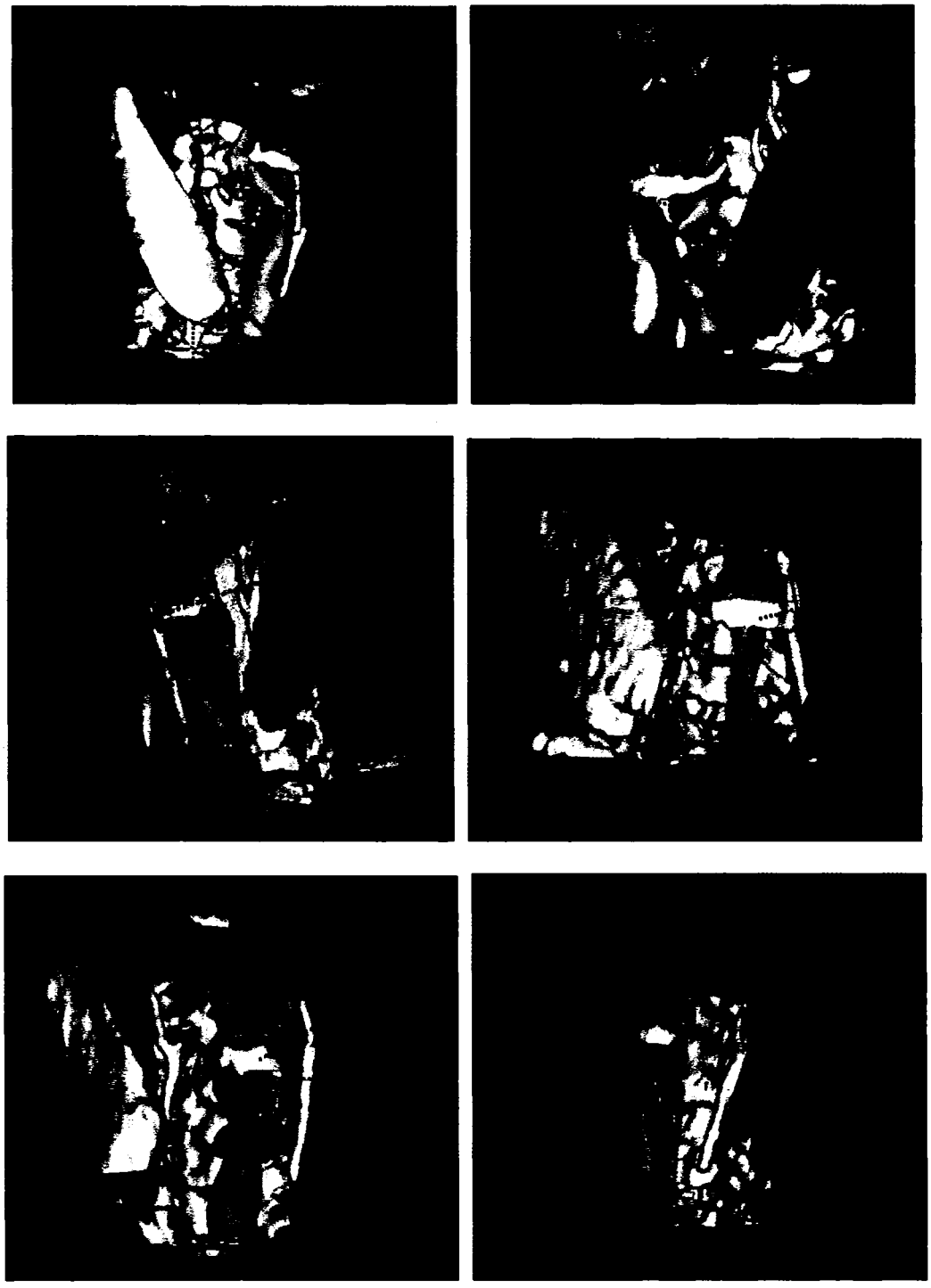

Figure 25: Examples of automatic segmentation results for selected subjects.

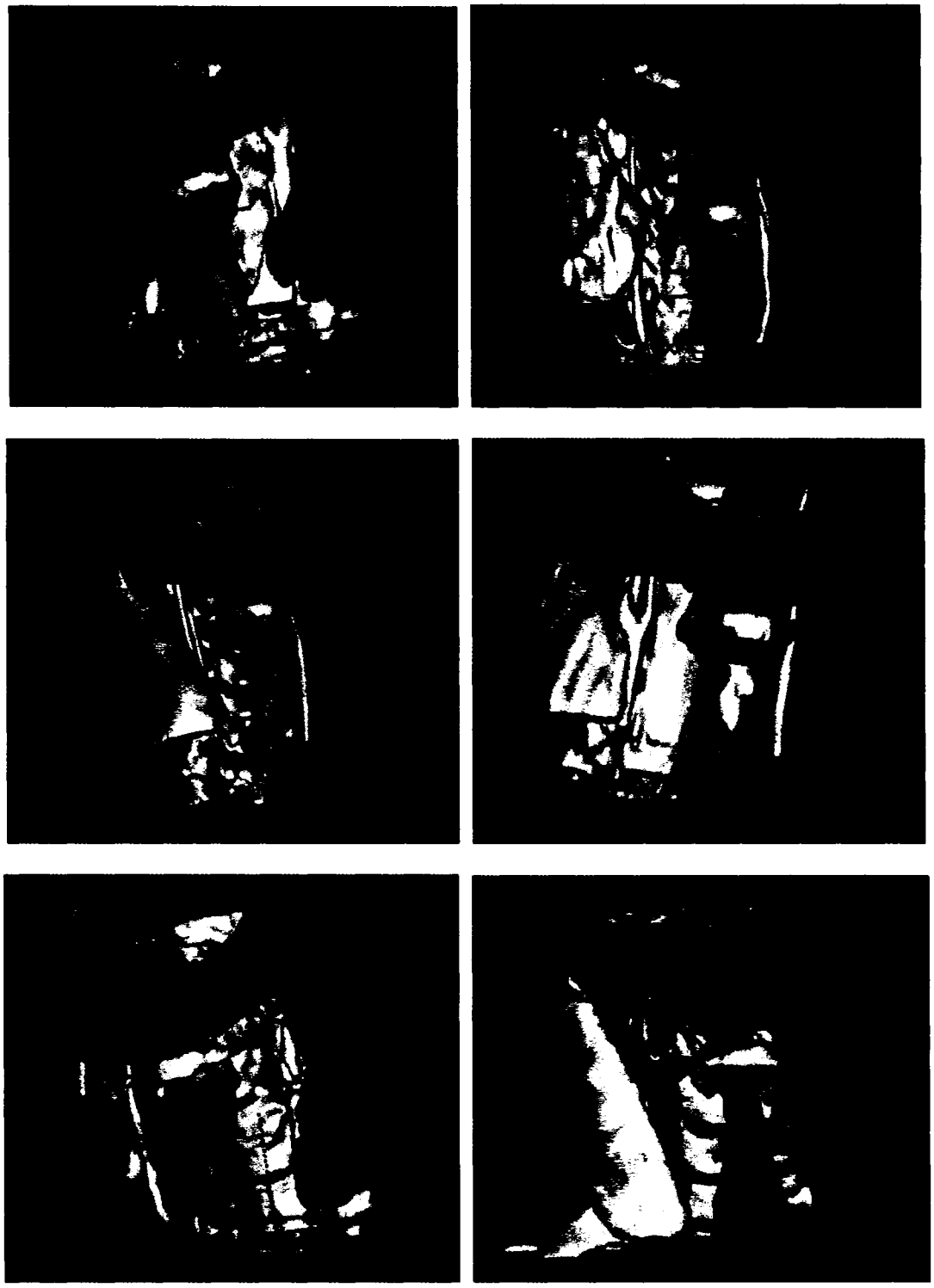

Figure 26: More examples of automatic segmentation results.

6.3 Image Registration Tool

We ran the image registration experiment with twenty sets of CT images, each of which is used as a reference and a target data set to align with every other image set. The permutation results in $20 \times (20 - 1) = 380$ total registration tests. We used the results of the Mattes method as the baseline to compare with the results of the new method.

Out of the 380 total tests, the Mattes method failed to converge in 13 cases while the proposed method succeeded in all cases. The average time to complete the registration improved by approximately 20%. Table 3 - 5 compares the success rate and convergence time of the two image registration method out of 380 inter-subject cases.

Table 3: Success rate comparison between Mattes and proposed method.

	Total cases	Successful registration cases	Success rate (%)
Mattes method	380	367	96.57%
Proposed method using landmark correspondence	380	380	100.00%

Table 4: Time of convergence comparison between Mattes and proposed method.

	Average time of convergence	Standard deviation time of convergence
Mattes method	32 minutes	6 minutes
Proposed method using landmark correspondence	26 minutes	5 minutes

Table 5: Time of convergence comparison between Mattes and proposed method.

Landmark method faster	Mattes method faster
326	54

In our experiments, selected lymph node regions are drawn as 2D contours on axial CT slices of 20 subjects chosen by resident physicians in University of Washington Radiation Oncology Department. 3D meshes of the lymph node regions are built from those 2D contours. We can quantitatively evaluate the results of the image registration process by measuring the distance between the two 3D meshes: reference lymph node region transformed into target space and corresponding region of the target subject. We measure the 3D Hausdorff distance and mean distance between the meshes by sampling the surface points. The Hausdorff distance between the projected lymph node region n based reference subject S_R and the expert drawn for a given target subject S_T can be defined as $D_H(TS_R, S_T, n)$, where T is transformation resulted from the image registration of S_R and S_T.

Figures 27 – 30 show comparisons of image registration results from the Mattes method and the proposed method incorporating the landmark correspondence. The horizontal axis represents the Hausdorff or mean distance between projected lymph node regions based on the reference model using image registration results from the Mattes method and corresponding expert drawn lymph node regions of the target subject. The vertical axis represents matching results using the proposed registration method. The diagonal dotted lines represent the points where the two measures are equal. The figures show overall improvement using the proposed registration method. Tables 6 – 9 compare the mean and standard deviation of results from two methods. The average Hausdorff distance improves as much as 25%, the average mean distance improves as much as 42%.

Figure 31 shows an example of the projected lymph node region contour based on the result of the image registration. The projected 3D lymph node regions are shown at the lower left 3D view. They are also overlaid on the target CT images

in axial, sagittal, and coronal views. The radiation oncologists can make adjustments to the suggested contours as needed.

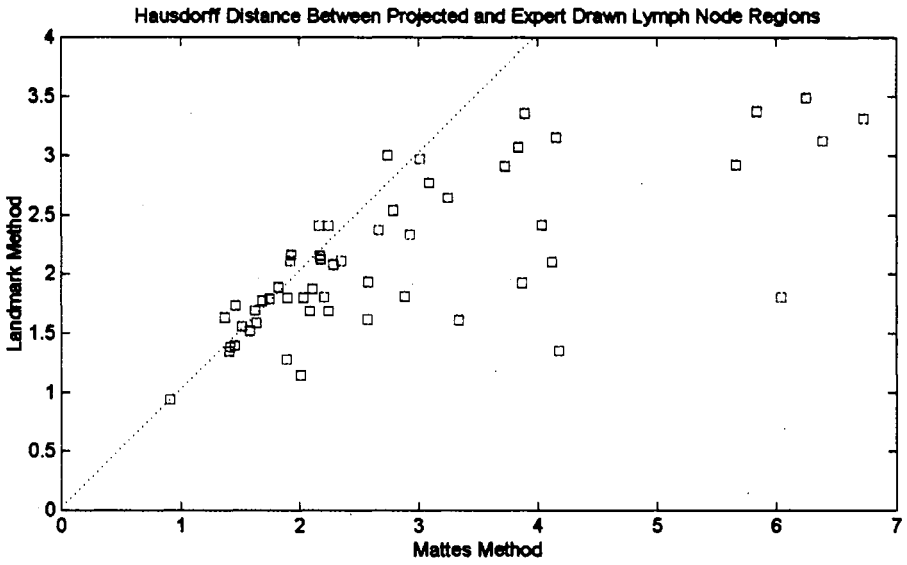

Figure 27: $D_H(TS_R, S_T, 1B)$ for all S_R, S_T. Hausdorff distance (in cm) between transformed reference mesh and target mesh for nodal region 1B. Comparison of image registration results from Mattes method and proposed landmark method.

Table 6: $D_H(TS_R, S_T, 1B)$ for all S_R, S_T. Hausdorff distance (in cm) between transformed reference mesh and target mesh for nodal region 1B.

	Average	Standard deviation
Mattes method	2.85	1.44
Proposed method using landmark correspondence	2.12	0.64

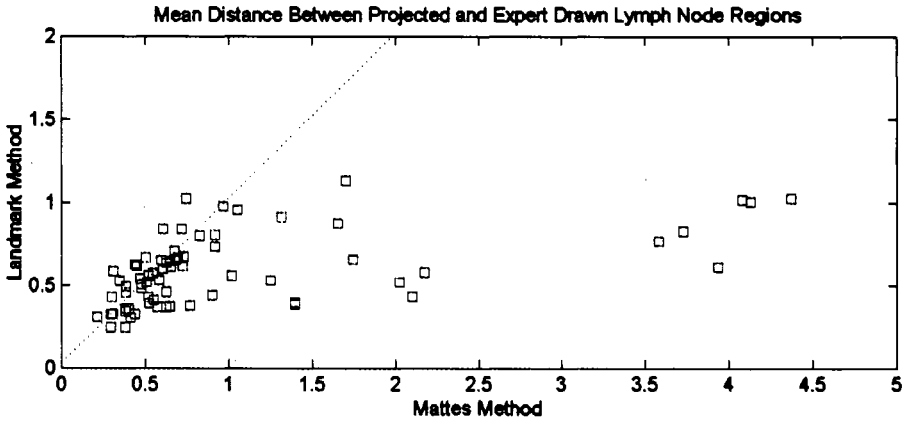

Figure 28: Mean distance (in cm) between transformed reference mesh and target mesh for nodal region 1B. Comparison of image registration results from Mattes method and proposed landmark method.

Table 7: Mean distance (in cm) between transformed reference mesh and target mesh for nodal region 1B.

	Average	Standard deviation
Mattes method	1.02	1.01
Proposed method using landmark correspondence	0.59	0.21

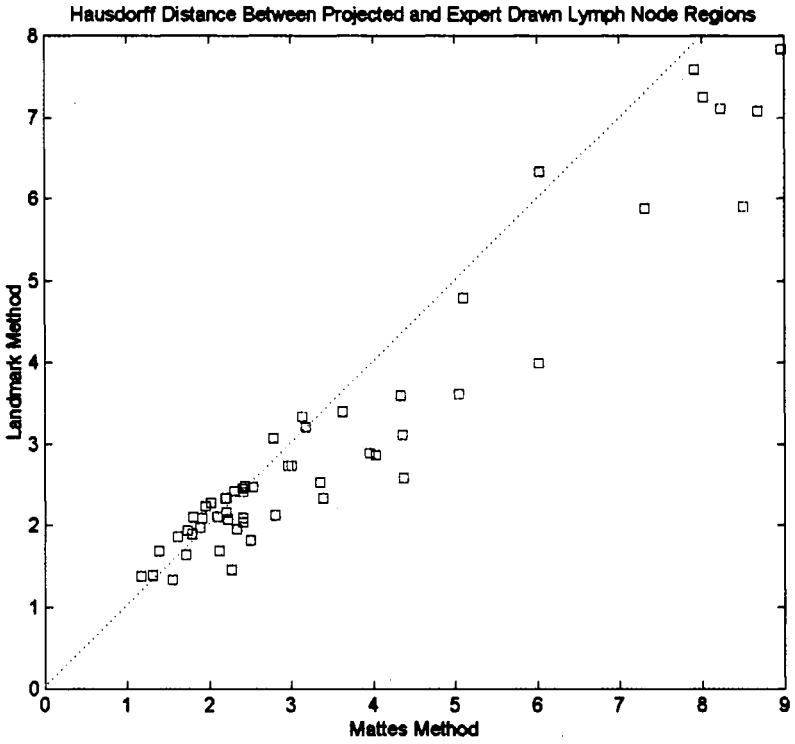

Figure 29: $D_H(TS_R, S_T, 2)$ for all S_R, S_T. Hausdorff distance (in cm) between transformed reference mesh and target mesh for nodal region 2. Comparison of image registration results from Mattes method and proposed landmark method.

Table 8: $D_H(TS_R, S_T, 2)$ for all S_R, S_T. Hausdorff distance (in cm) between transformed reference mesh and target mesh for nodal region 2.

	Average	Standard deviation
Mattes method	3.48	2.15
Proposed method using landmark correspondence	3.07	1.75

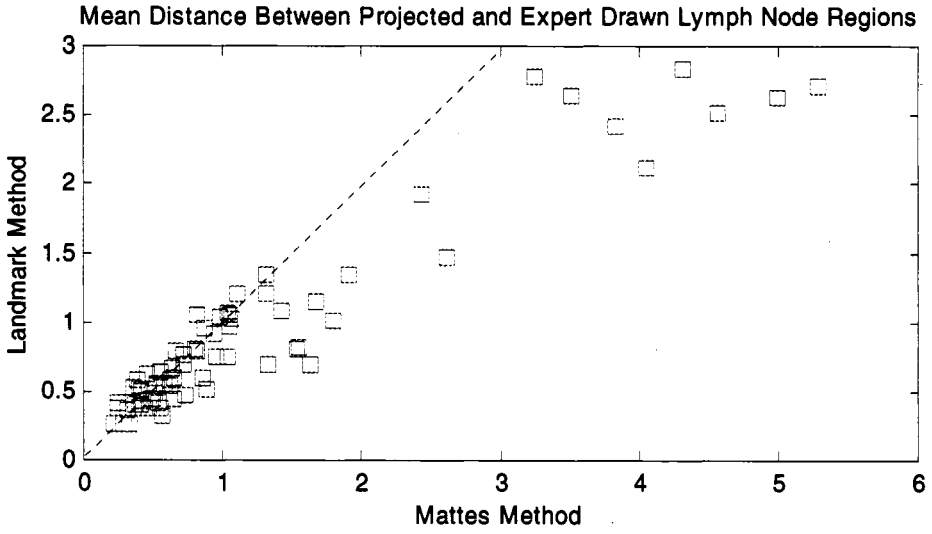

Figure 30: Mean distance (in cm) between transformed reference mesh and target mesh for nodal region 2. Comparison of image registration results from Mattes method and proposed landmark method.

Table 9: Mean distance (in cm) between transformed reference mesh and target mesh for nodal region 2.

	Average	Standard deviation
Mattes method	1.21	1.20
Proposed method using landmark correspondence	0.91	0.68

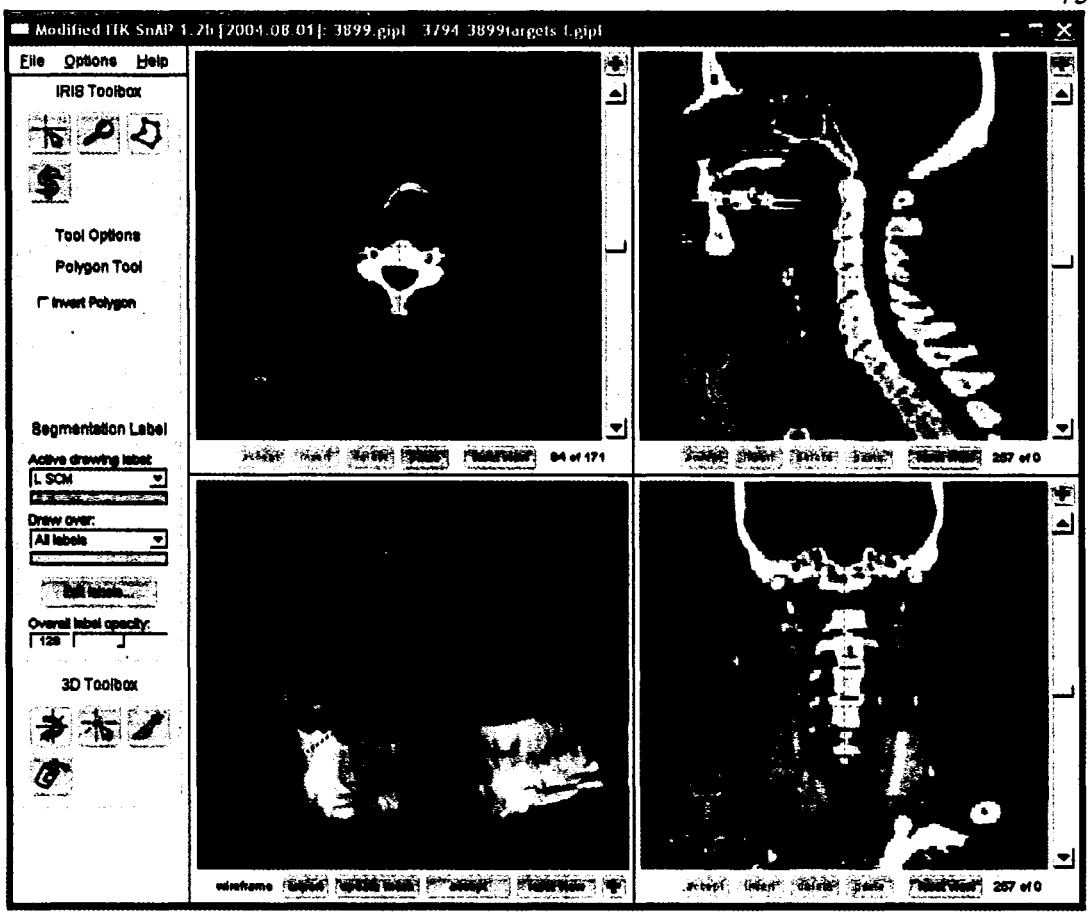

Figure 31: Sample result of lymph node region projection.

While the proposed method improves the overall results, it does not decrease the Hausdorff or mean distance in every case. One reason is that some expert drawn contours are not consistent with the image-based classification. Figure 32 shows an example of a 1B region where its caudal boundary is two slices or 0.75 cm below the hyoid. Figure 33 shows the result of an oversized reference lymph node 1B region whose the caudal boundary is too low and the projected lymph node region is also oversized.

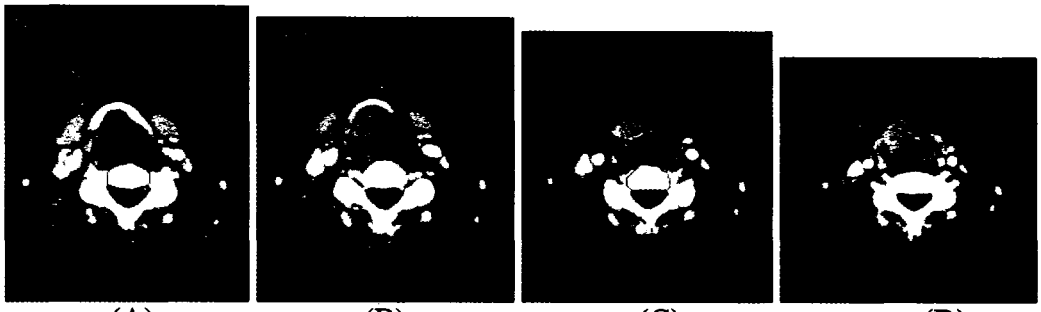

(A) (B) (C) (D)

Figure 32: An example of lymph node regions that are not drawn according to the image-based guideline. Slices A – D are in the order of cranial to caudal direction. Slice thickness is 0.375 cm.

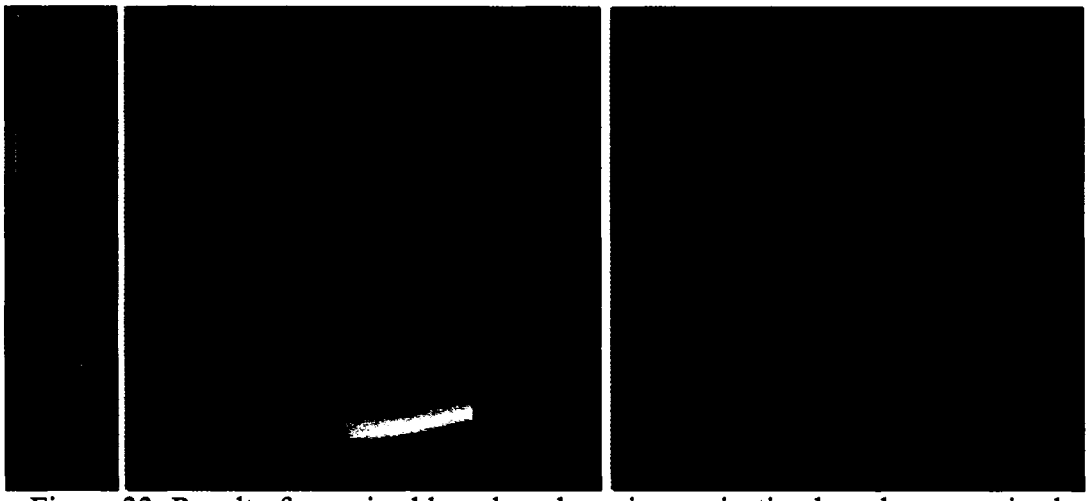

Figure 33: Result of oversized lymph node region projection based on oversized reference model. The right picture is the target expert drawn region, and the left picture is the projected region for which the red/yellow portion of the surface has greater distance to the target region.

6.4 Similarity Measurement

For the twenty selected subjects with lymph node region data, we measure their feature-vector-space distance. For each target subjects, we rank all of the reference subjects by two separate measurements:

- Ranking R_I ranks by Hausdorff distance D_H between projected lymph node region and corresponding expert drawn region of target subject. The smallest value has the highest rank. This represents the ranking of similarity according to the image registration results, assuming that the more similar reference image aligns better with the target image.
- Ranking R_F ranks by distance measure in the feature vector space D_F in Equation (32). The smallest value has the highest rank. This represents the ranking of similarity according to the geometrical features.

To validate the similarity ranking based on geometrical features, we compare it to the ranking based on image registration results for each target subject. We define $R(i, S_T)$ as the ith reference subject in the ranking for the target subject S_T. For 81% of the instances, $R_F(1, S_T)$ is the same as $R_I(1, S_T)$, meaning that 81% of the most similar reference subjects according to geometrical features matches the one that align best with the target according to image registration. In other words, the probability $P(R_I(1, S_T) = R_F(1, S_T) \mid R_F(1, S_T)) = 0.81$. Additionally, $R_F(1, S_T)$ has 96% chance of matching one of the top three subjects in R_I. Table 10 summarizes the probabilities of the most similar subject based on geometric features matching subjects that align best with the target.

Table 10: Probabilities of the most similar subject based on geometric features matching subjects that align best with target.

	$x = 1$	$x = 2$	$x = 3$	$x > 3$
$P(R_I(x, S_T) = R_F(1, S_T) \mid R_F(1, S_T))$, where $R_F(1, S_T)$ is the most geometrically similar reference subject	81%	11%	4%	4%

As we previously defined $D_H(TS_R, S_T, n)$ as the Hausdorff distance between the projected lymph node region n based reference subject S_R and the expert drawn for a given target subject S_T. The Hausdorff distance based on the most similar reference subject in the feature space $R_F(1, S_T)$ becomes $D_H(TR_F(1, S_T), S_T, n)$. Table 11 compares the image registration results of the most similar reference subject to results of all 380 test cases listed in previous section. The average D_H of 1.28 cm is approximately 50% improvement over the average of all test cases.

Table 11: Compare image registration results based on most similar reference subject and results based on all test cases.

	Average	Standard deviation
$D_H(TR_F(1, S_T), S_T, n)$ for all S_T and n, based on most similar reference subjects of each target subject.	1.28	0.31
$D_H(TS_R, S_T, n)$ for all S_R, S_T and n, based on all combinations of reference and target subjects.	2.59	0.90

Figures 34 - 40 shows the correlation between the proposed distance measure and the result of 3D deformable image registration for selected target patients. The vertical axis shows the Hausdorff distance D_H between the transformed 3D mesh of the reference model lymph nodal region and the corresponding mesh of the test model using the transformation produced by the 3D deformable image registration. The horizontal axis represents the distance measurement, or the weighed Euclidian distance D_F between the test and reference model properties in the feature vector space. The leftmost point in each graph represent the most similar reference subjects $R_F(1, S_T)$ which matches to one of the subjects that align well with the target, i.e. with the shortest Hausdorff distance $D_H(TR_F(1, S_T), S_T, n)$ compares to others. Table 12 also shows statistical analysis of the correlation coefficients of D_F and D_H for all the target subjects S_T.

Table 12: Correlation coefficients of D_F and D_H for all the target subjects S_T

	Average	Standard deviation
Correlation_coefficient(D_H, D_F) for all S_T.	0.61	0.19

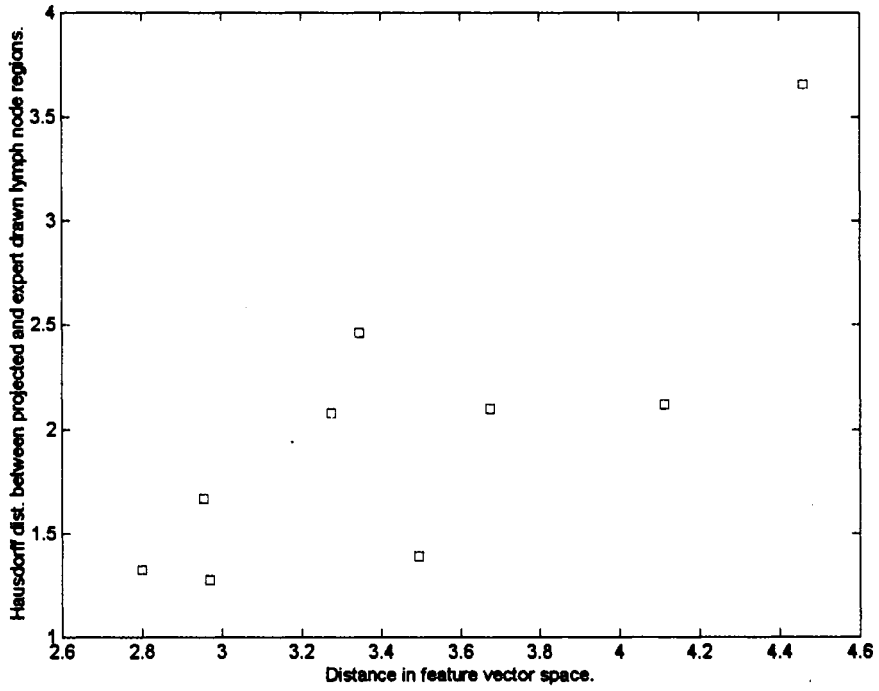

Figure 34: Example of correlation between the proposed distance measure D_F in feature vector space (horizontal axis) and the Hausdorff distance D_H between the projected lymph node regions resulting from registration and those hand-drawn by experts (vertical axis).

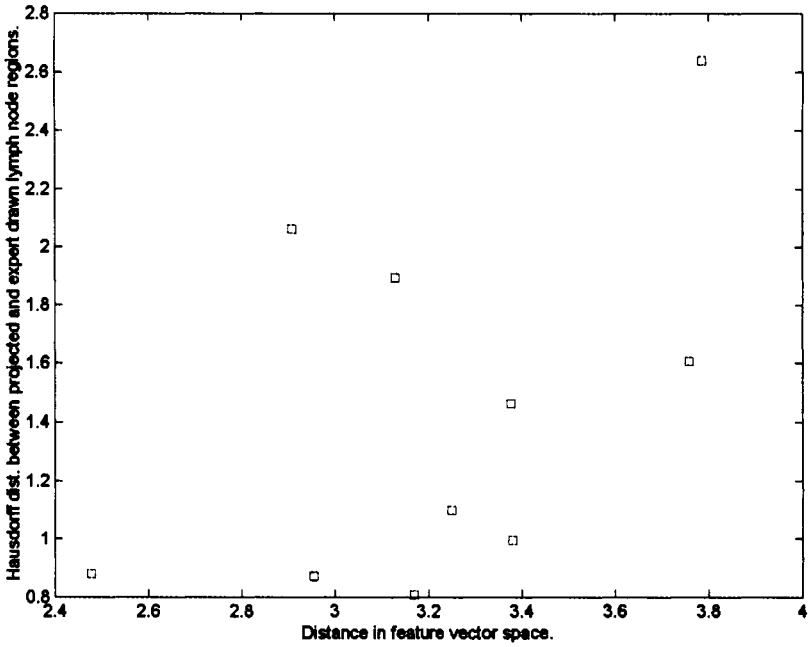

(A)

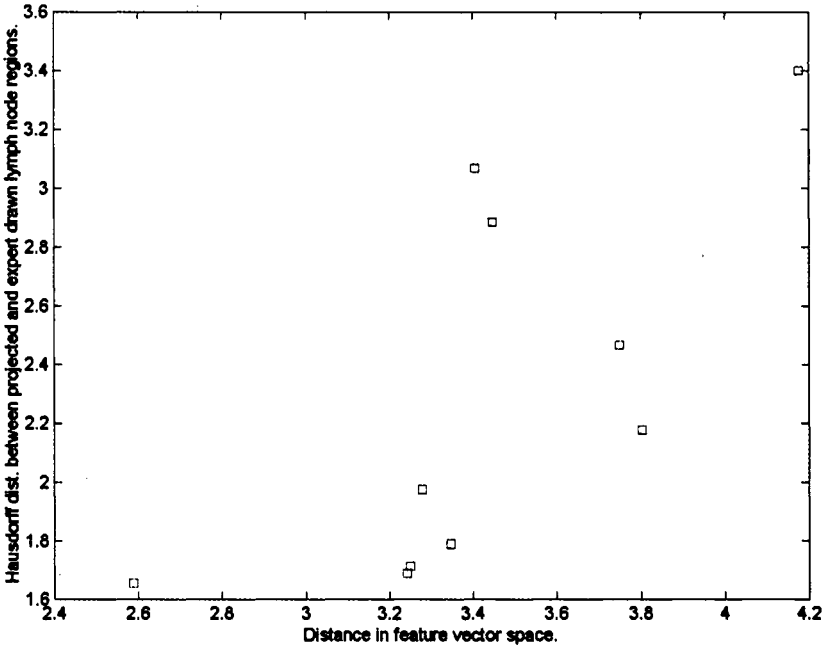

(B)

Figure 35: More examples of correlation between D_F and D_H.

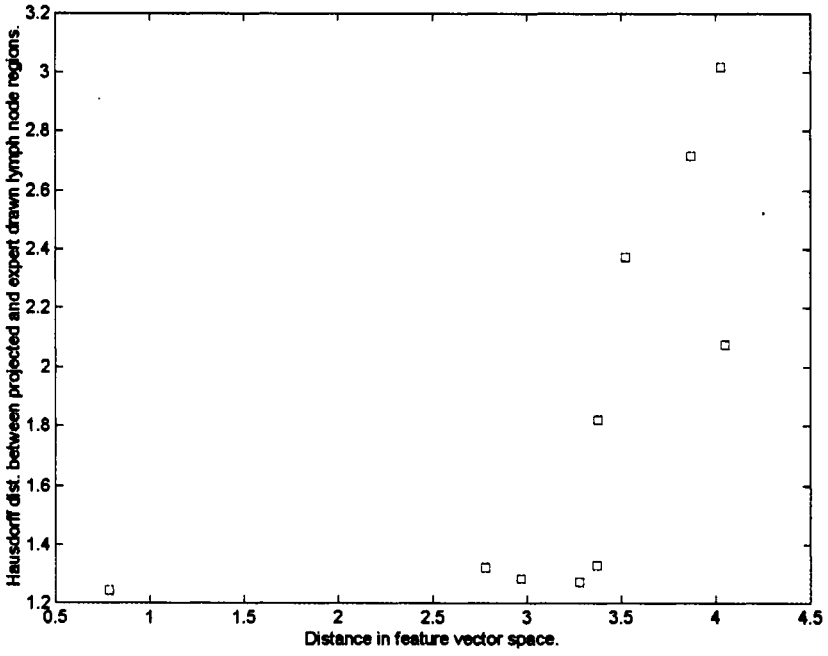

(A)

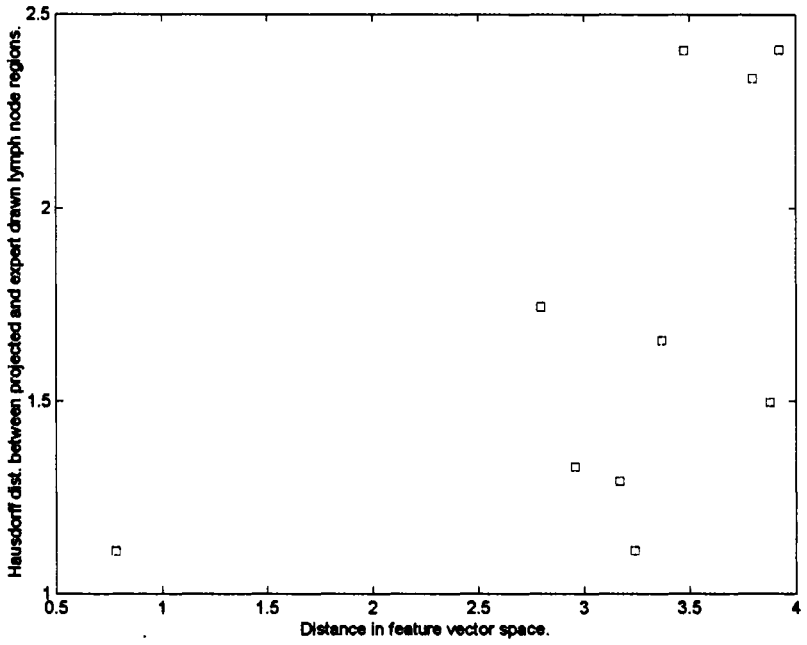

(B)

Figure 36: More examples of correlation between D_F and D_H.

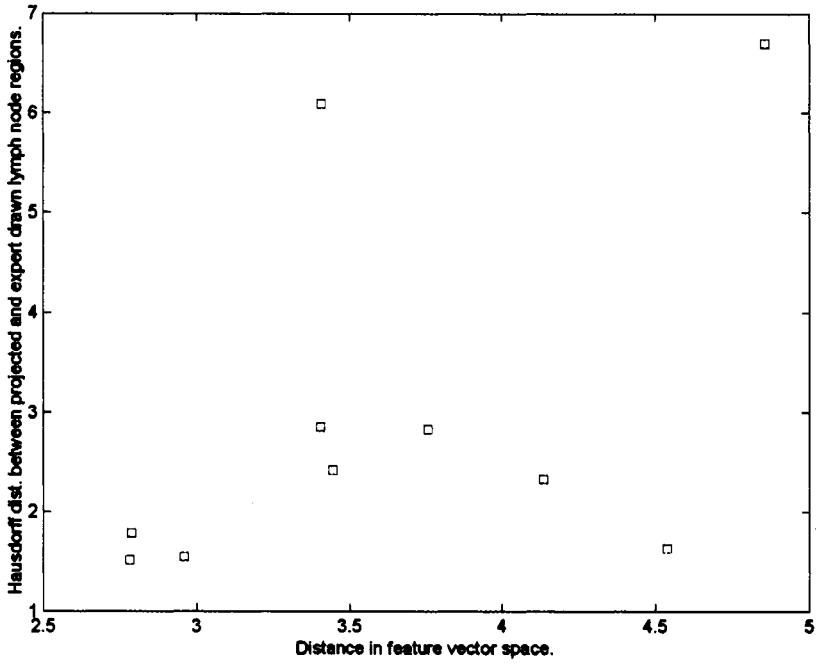

(A)

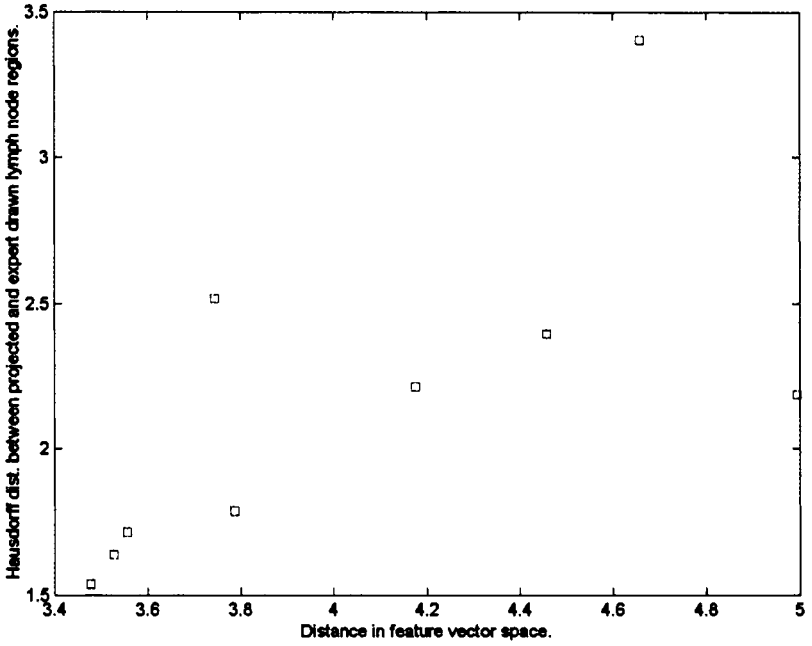

(B)

Figure 37: More examples of correlation between D_F and D_H.

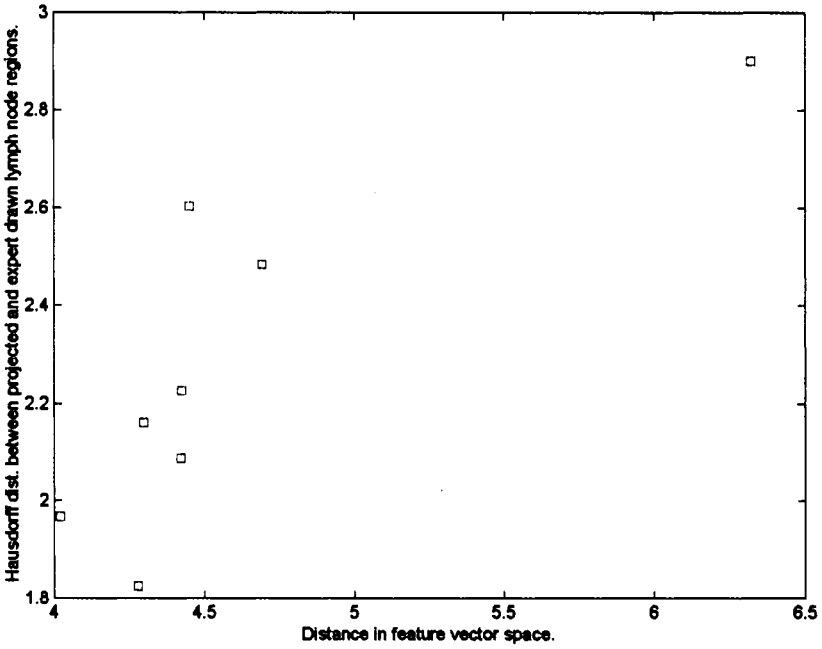

(A)

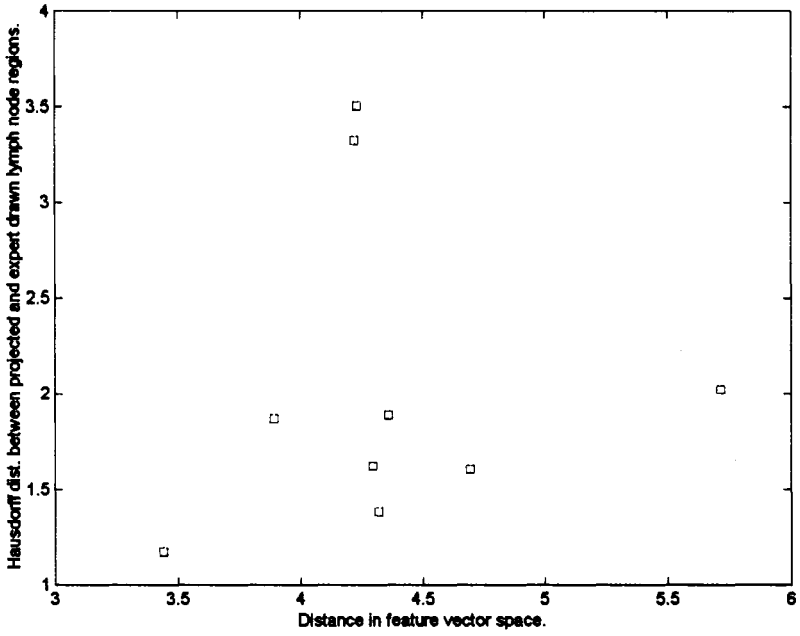

(B)

Figure 38: More examples of correlation between D_F and D_H.

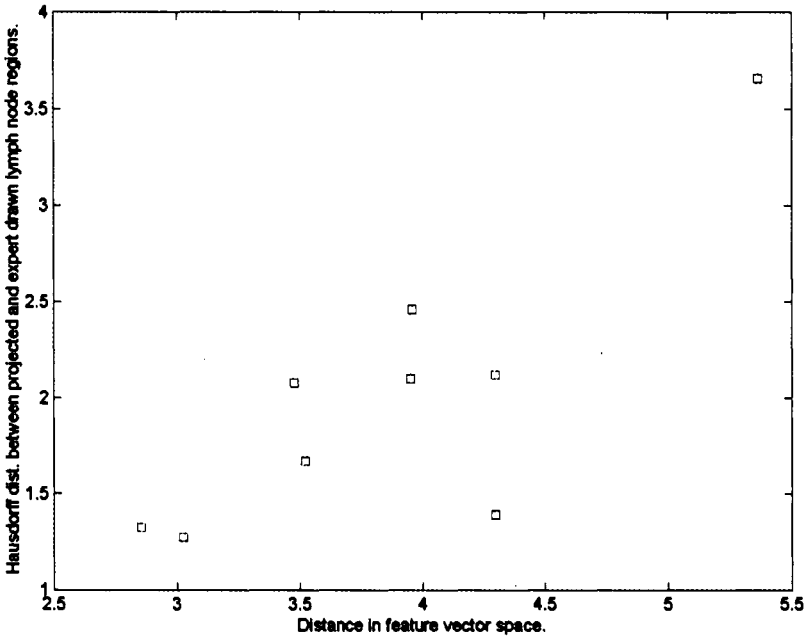

(A)

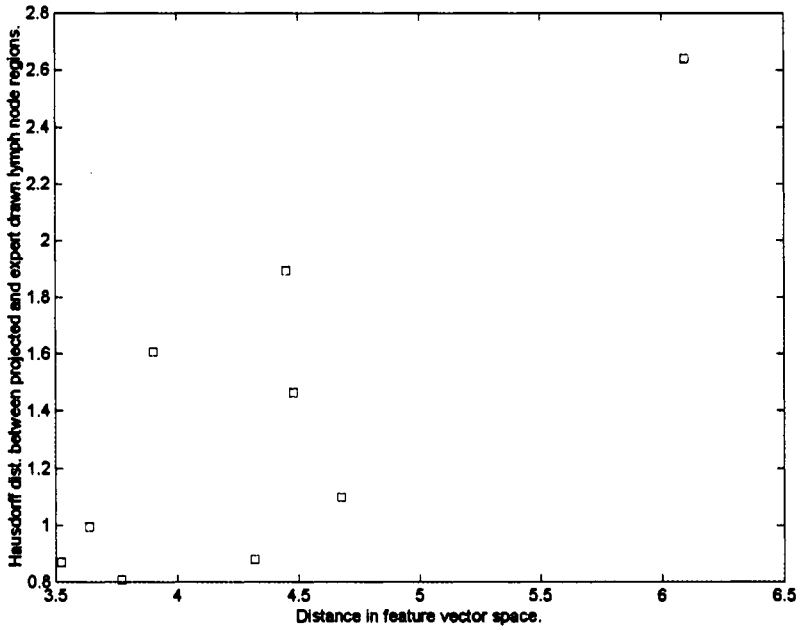

(B)

Figure 39: More examples of correlation between D_F and D_H.

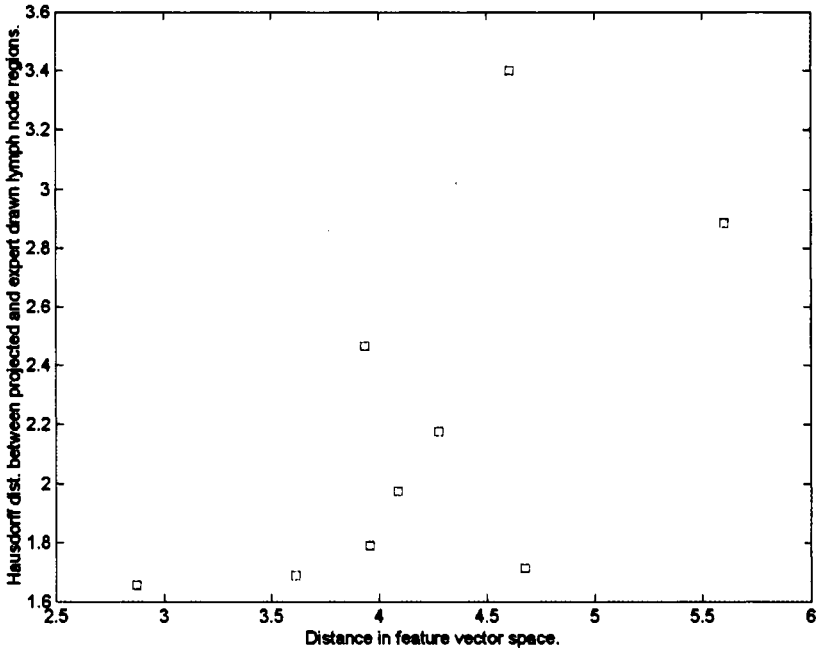

(A)

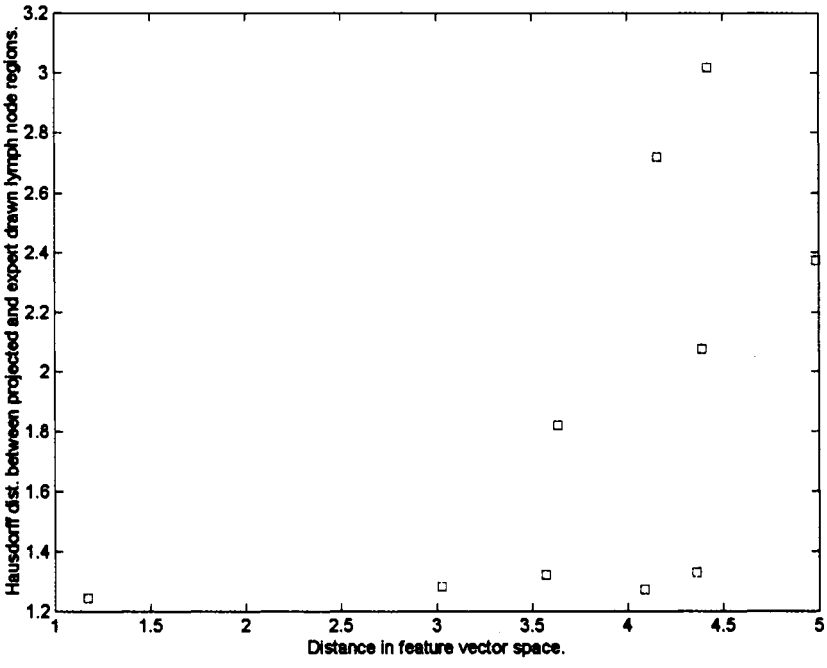

(B)

Figure 40: More examples of correlation between D_F and D_H.

6.5 Qualitative Evaluation

The projected lymph node regions can be evaluated qualitatively by being superimposed on the target subject's CT images. Each region can be evaluated visually on its alignment to the target subject's anatomy and the boundary structures of the lymph node region. Figure 41 compares projected lymph node regions to the expert drawn regions, each region is color coded. Rows A - C are sample CT slices from superior to inferior locations of the same target subject. Column 1 on the left shows projected regions from Mattes' method; column 3 on the right shows results from the new method using landmark information. Regions in column 2 are drawn by a radiation oncologist. These projected lymph regions are reviewed by the radiation oncologist and considered to be close to clinically acceptable. Results from the new method in column 3 generally show better alignment on axial slices. Row B also shows better projection in the caudal boundary of region 2 in column 3. The results from the Mattes' method are more generous in certain areas in covering muscle tissues. Although it may be considered harmless today but it can be less desirable as the precise lymph node region contours become more important in the future when more aggressive treatments are used in IMRT.

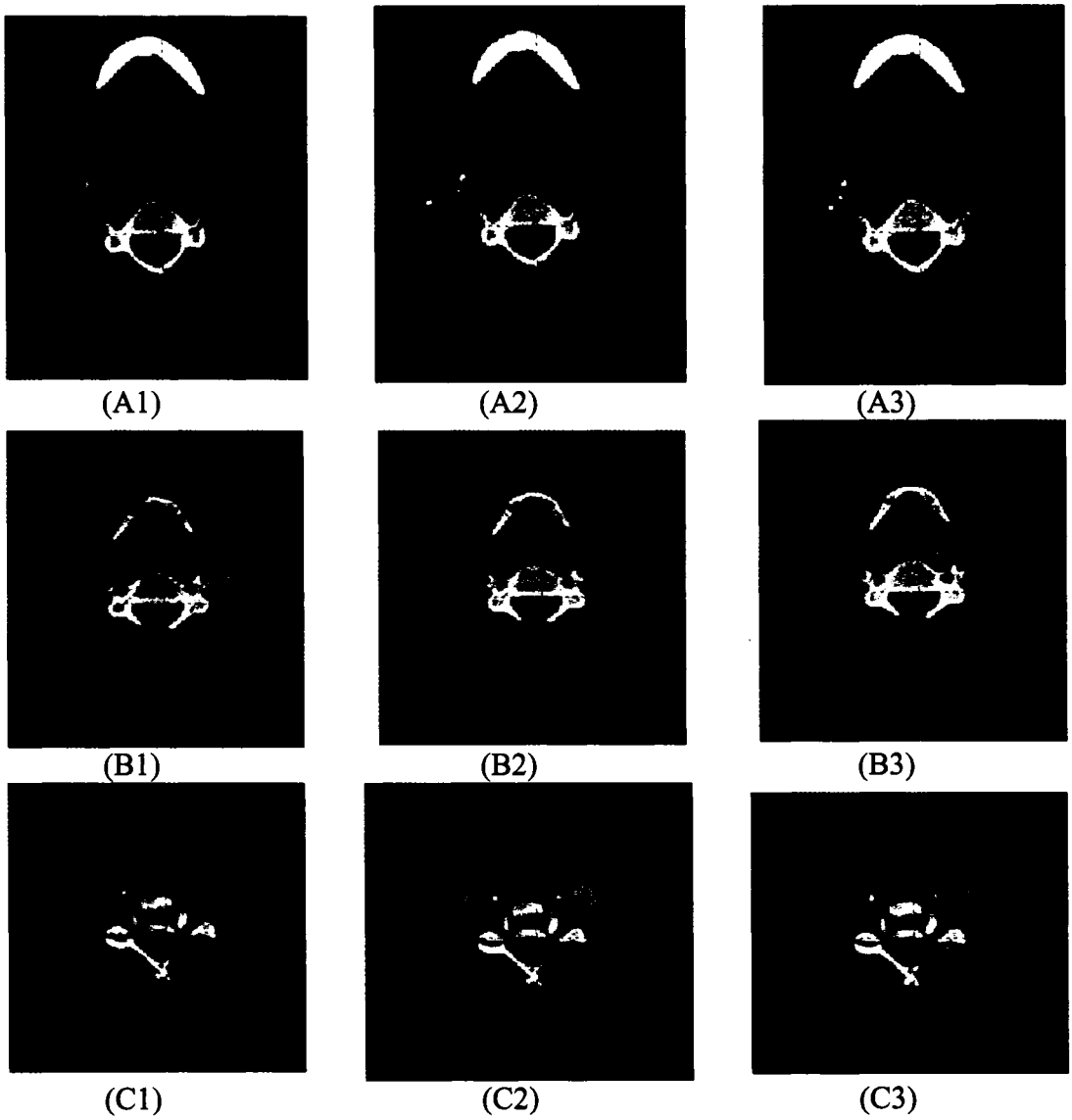

Figure 41: Comparison between projected lymph node regions and expert drawn regions.

Chapter 7 Conclusion

Automatic segmentation of CT images is a challenging problem for which a knowledge-based approach can be useful in certain classes of applications. For a head and neck radiation therapy planning system which looks for a known set of landmarks, it may produce sufficient results. The image registration technique also provides a way to potentially automate the lymph node region contouring process for radiation therapy planning. While the alignment of the projected lymph node contours on the target image are close enough to suggest the technique has promise, the results do not conform to clinical criteria. In this chapter we summarize the contributions of this thesis and suggest directions for future research.

7.1 Contributions

This work has the following contributions, which have been published in various conferences.

1. It is the first system of its kind that attempts to automate the process of identifying Clinical Target Volume for head and neck cancer radiation treatment by projecting lymph node regions using inter-subject image registration techniques. Published in Proceeding of American Medical Informatics Association Fall Symposium 2002 [7]. Abstract also published in International Journal of Radiation Oncology, Biology and Physics [69].
2. We proposed a novel knowledge based segmentation method which combines 2D and 3D two steps iterative and progressive process. Published in Proceeding of the 19th IEEE International Symposium on Computer-Based Medical Systems 2006 [58].
3. We proposed a hybrid image registration technique using landmark correspondences in conjunction with voxel based mutual information method.

Published in Proceeding of 2006 IEEE International Symposium on Biomedical Imaging [57].

4. We proposed a patient similarity measurement using the 3D geometrical relationship between anatomical structures in addition to 3D shape descriptors of the structures. Published in Proceeding of 2007 IEEE International Symposium on Biomedical Imaging [67].

7.2 Future Work

We would like to have these software tools evaluated at a clinical environment for head and neck cancer patients who undergo 3D conformal radiation therapy where the computer generated target contours can be compared to the expert drawn contours of more target subjects. The tools can be generalized for treatment of other types of cancer. We will also investigate other types of medical image applications that can benefit from these tools and methods, for instance, cranial defect surface post operative tracking for patients with Craniosynostosis.

We will investigate methods which can potentially improve the results of each component. The auto-segmentation component can benefit from more data in the domain knowledge base. We can also reduce the error rate by adding post 3D active contouring validation to identify incorrect segmentation by its geometric and structure features, and backtracking logic to re-segment the target structure. Applications such as automatic tumor identification and image based differential diagnosis can also be developed by observing shape and intensity abnormality or asymmetry of these anatomical structures.

We will investigate other potential features that can be incorporated in the similarity measure for better results, including more anatomical structures and their

relationships. We will expand the test data set to refine and improve the similarity measure.

These software tools shall be integrated with the research work by Benson *et al.* [70] which predicts the regional lymphatic involvement of head and neck squamous cell carcinoma based on primary tumor location and T-stage. By using the lymphatic prediction, we can delineate proper target volumes for given primary tumor location and T-stage.

Bibliography

[1] R.T. Greenlee, T. Murray, S. Bolden, and P.A. Wingo, "Cancer Statistics", *CA-A Cancer J. Clin..*, 2000, vol. 50, pp. 7-33.

[2] K.S.C. Chao, F.J. Wippold, G. Ozyigit, B.N. Tran, and J.F. Dempsey, "Determination and Delineation of Nodal Target volumes for Head-and-Neck Cancer Based on Patterns of Failure in Patients Receiving Definitive and Postoperative IMRT," *Int. Journal of Radiation Oncology Biol. Phys.*, 2002, vol. 53, pp. 1174-1184.

[3] A. Krueger, C. Tietjen, J. Hintze, B. Preim, I. Hertel, and G. Strau, "Interactive Visualization for Neck Dissection Planning", *Proc. of the IEEE/Eurographics Symposium on Visualization (EuroVis)*, 2005, pp. 295-302.

[4] M. Kobashi and L.G. Shapiro, "Knowledge-based Organ Identification from CT Images", *Pattern Recognition*, 1995, vol. 28, pp. 475-491.

[5] D.W.W. Williams, "An Imager's Guide to Normal Neck Anatomy", *Seminars in Ultrasound, CT and MR*, 1997, vol. 18, pp. 157-181.

[6] W.R.K. Smoker, "Normal Anatomy of the Infrahyoid Neck: an Overview", *Seminars in Ultrasound, CT and MR*, 1991, vol. 12, pp. 192-203.

[7] C. Teng, M.M. Austin-Seymour, J. Barker, I. Kalet, and L.G. Shapiro, "Head and Neck Lymph Node Region Delineation 3D CT Image Registration", *Proc. American Medical Informatics Assoc. Fall Symp.*, 2002, pp. 767-771.

[8] International Commission on Radiation Units and Measurements. Prescribing, Recording and Reporting Photon Beam Therapy. Bethesda, MD, International Commission on Radiation Units and Measurements, 1993. Report 50.

[9] International Commission on Radiation Units and Measurements. Prescribing, Recording and Reporting Photon Beam Therapy (Supplement to ICRU Report 50). Bethesda, MD, International Commission on Radiation Units and Measurements, 1999. Report 62.

[10] I.J. Kalet, J.P. Jacky, M.M. Austin-Seymour, S.M. Hummel, K.J. Sullivan, J.M. Unger, "Prism: A new approach to radiotherapy planning software," *Int. J. of Radiation Oncology, Biology and Physics*, vol. 36, pp. 451–461, 1996.

[11] P.M. Som, H.D. Curtin, A. Mancuso, "An imaging based classification for the cervical nodes designed as an adjunct to recent clinical based nodal classification," *Archives of Otolaryngol-Head and Neck Surery.*, vol. 125, pp. 388–396, Apr. 1999.

[12] Som PM, Curtin HD, Mancuso A. Imaging-based classification for evaluation of neck metastatic adenophy. American Journal of Roentgenology 174, March 2000.

[13] C. Harlow and S. A. Eisenbeis, "The analysis of radiographic images," *IEEE Trans Computers*, C-22, pp. 679-688, 1973.

[14] P. G. Selfridge and J. M. S. Prewitt, "Organ detection in abdominal computerized tomography scans: application to the kidney," *Computer Graphics Image Process*, vol. 15, pp. 265-278, 1981.

[15] N. Karssemeijer, L. J. von Esking, and E. G. Eijkman, "Recognition of organs in CT-image sequences: a model guided approach," *Comput. Biomed. Research*, vol. 21, pp 434-448, 1988.

[16] J. F. Brinkley, "Representing biological objects as geometric constraint network," *Proc AAAI Spring Symposium Series: Artificial Intelligence Medicine, Stanford University*, pp. 7-8, 1988.

[17] M. Kobashi and L.G. Shapiro, "Knowledge-based Organ Identification from CT Images", *Pattern Recognition*, 1995, vol. 28, pp. 475-491

[18] L. Staib and J. Duncan, "Boundary finding with parametrically deformable models," PAMI, vol. 14(11), pp. 1061-1075, 1992.

[19] M. Kass, A. Witkin, and D. Terzopoulos, "Snakes: active contour models," *International Journal Computer Vision*, vol. 1(4), pp. 321-331, 1988.

[20] G. Szekely, A. Kelemen, C. Brechbuhler, and G. Gerig, "Segmentation of 2D and 3D objects from MRI volume data using constrained elastic deformations of flexible Fourier contour and surface models," *Medical Image Analysis*, vol. 1(1), pp. 19-34, 1996.

[21] J. B. A. Maintz and M. A. Viergever, "A survey of medical image registration," *Medical Image Analysis*, vol. 2(1), pp. 1-36, 1998.

[22] Studholme, C., Hill, D. L. G., and Hawkes, D. J. Incorporating connected region labeling into automated image registration using mutual information. IEEE Proceedings of MMBIA 1996, pp. 23-31, 1996.

[23] Bookstein FL. Principle warps: thin-plate splines and the decomposition of deformations. IEEE Trans Pattern Analysis Mach Intel 1989; 11 (6): 567-585.

[24] Kim B, Boes JL, Frey KA, and Meyer CR. Mutual information for automated unwarping of rat brain autoradiographs. Neuroimage 1997; 5: 31-40.

[25] G.E. Christensen, A.A. Kane, J.L. Marsh, and M.W. Vannier, "Synthesis of an individual cranial atlas with dysmorphic shape," *Mathematical methods in biomedical image analysis*, pp. 309–318, 1996.

[26] Christensen, GE, Joshi SC, and Miller MI. Volumetric Transformation of Brain Anatomy. IEEE Trans Medical Imaging 1997; 16 (6): 864-877.

[27] Thompson P., Toga AW. A surface-based technique for warping three-dimentional images of the brain. IEEE Trans Med Imaging 1996; 15 (4): 402-417.

[28] Davatzikos C, Bryan RN. Using a deformable surface model to obtain a shape representation of the cortex. IEEE Trans Medical Imaing 1996; 15 (6): 785-795.

[29] Davatzikos C. Spatial transformation and registration of brain images using elastically deformable models. Computer Vision and Image Understanding 1997; 66 (2): 207-222.

[30] Davatzikos C. Nonlinear registration of brain images using deformable models. IEEE Proceedings of MMBIA 1996, pp. 94-103.

[31] Davatzikos C, Prince JL, and Bryan RN. Image registration-based on boundary mapping. IEEE Trans Medical Imaging 1996; 15 (1): 112-115.

[32] Pluim JPW, Maintz JBA, and Viergever MA. Image registration by maximization of combined mutual information and gradient information. IEEE Trans Medical Imaging 2000; 19 (8): 809-814.

[33] Studholme, C., Hill, D. L. G., and Hawkes, D. J. Automated three-dimensional registration of MR and PET brain images by multiresolution optimization of voxel similarity measures. Medical Physics 1997; 24 (1): 25-35.

[34] Kjems U, Strother SC, Anderson J, Law I, and Hansen LK. Enhancing the multivariate signal of [^{15}O] water PET studies with a new nonlinear neuroanatomical registration algorithm. IEEE Trans Medical Imaging 1999; 18 (4): 306-319.

[35] Christensen GE, Miller MI, and Vannier WM. Individualizing neuroanatomical atlases using a massively parallel computer. IEEE Computer 1996; 29 (1): 32-38.

[36] D. Mattes, D.R. Haynor, H. Vesselle, T.K. Lewellen, and W. Eubank, "PET-CT Image Registration in the Chest Using Free-form Deformations," *IEEE Transaction on Medical Imaging*, vol. 22, pp. 120-128, Jan. 2003.

[37] Studholme C, Hill DLG, Hawkes DJ. An overlap invariant entropy measure of 3d medical image alignment. Pattern Recognition 32:71–86, 1999.

[38] Maes F, Collignon A, Vandermeulen D, Marchal G, Suetens P. Multimodality image registration by maximization of mutual information. IEEE Transactions on Medical Imaging 16:187–198, 1997.

[39] Viola P, Wells III WM. Alignment by maximization of mutual information. International Journal of Computer Vision 24:137–154, 1997.

[40] Thevenaz P, Unser M. Spline pyramids for intermodal image registration using mutual information. Proceeding of the SPIE 3169:236–247, 1997.

[41] M. Unser A. Aldroubi ME. Fast b-spline transforms for continuous image representation and interpolation. IEEE Transaction on Pattern Analysis and Machine Intelligence 13:277–285, March 1991.

[42] C. Zhu, R. Byrd, P. Lu, and J Nocedal. L-BFGS-B - Fortran Subroutines for Large-Scale Bound Constrained Optimization. Technical Report. 1994.

[43] National Library of Medicine. Visible human project. RFP NLM-90-114/SLC, June 1990.

[44] Rosse C, Shapiro LG, Brinkley JF. The digital anatomist foundational model: Principles for defining and structuring its concept domain. In Proceedings of the American Medical Informatics Association (AMIA) Fall Symposium. 1998:820–824.

[45] E. Keppel. Approximating complex surfaces by triangulation of contour lines. IBM J. Res. Develop., 19:2-11. January 1975.

[46] D. Meyers, S. Skinner, and K. Sloan. Surfaces from contours. In ACM Transactions on Graphics, 11(3):228-258. July 1994.

[47] N. Aspert, D. Santa-Cruz, and T. Ebrahimi. MESH: Measuring Errors Between Surfaces Using the Hausdorff Distance. In Proc. of the IEEE International Conference in Multimedia and Expo (ICME) 2002, vol. 1, pp. 705-70. August 2002.

[48] National Institute of Mental Health. Human Brain Project.

[49] C.R. Shelton, "Morphable Surface Models," *International Journal of Computer Vision*, vol. 38, pp. 75-91, 2000.

[50] N. Aspert, D. Santa-Cruz, and T. Ebrahimi. "MESH: Measuring Errors Between Surfaces Using the Hausdorff Distance," *Proc. of the IEEE Int. Conference in Multimedia and Expo (ICME) 2002*, vol. 1, pp. 705-70. Aug. 2002.

[51] Maes F, Collignon A, Vandermeulen D, Marchal G, and Suetens P. Multimodality image registration by maximization of mutual information. IEEE Trans Medical Imaging 1997; 16 (2): 187-198.

[52] Robbins KT, Medina JE, Wolfe GT, et at, "Standardizing neck dissection terminology. Official report of the Academy's Committee for Head and Neck Surgery and Oncology," *Archives of Otolaryngology – Head and Neck Surgery*, vol. 117, pp. 601-605, June 1991.

[53] H. Muller, M. Nicolas, D. Bandon, and A Geissbuhler, "A review of content-based image retrieval systems in medical applications – clinical benefits and future directions," *International Journal of Medical Informatics*, vol. 73, pp. 1-23, 2004.

[54] W. Zhang, S. Dickinson, S. Sclaroff, J. Feldman, and S. Dunn, "Shape-based indexing in a medical image database," *Proc. IEEE Workshop on Biomedical Image Analysis*, pp. 221-230, 1998.

[55] G. P. Robinson, H. D. Targare, J. S. Duncan, and C. C. Jaffe, "Medical image collection indexing: shape-based retrieval using KD-trees," *Computerized Medical Imaging and Graphics*, vol. 20, pp. 209-217, 1996.

[56] S. Aksoy, and R. M. Haralick, "Probabilistic vs. geometric similarity measures for image retrieval," *Proc. IEEE Conf. on Computer Vision and Pattern Recognition (CVPR)*, vol. 2, pp. 357-362, June 2000.

[57] C. Teng, L. G. Shapiro, and I. Kalet, "Head and neck lymph node region delineation using a hybrid image registration method," *Proc. 2006 IEEE International Symposium on Biomedical Imaging*, vol. , pp. 462-465, April 2006.

[58] C. Teng, L. G. Shapiro, and I. Kalet, "Automatic segmentation of neck CT images," *Proc. 19th IEEE International Symposium on Computer-Based Medical Systems*, vol. , pp. , June 2006.

[59] P. Min, J.A. Halderman, M. Kazhdan, and T.A. Funkhouser, "Early experiences with a 3D model search engine", in *Web3D Symposium*, pp. 7-18, March 2003.

[60] D.Y. Chen, X.P. Tian, Y.T. Shen, and M. Ouhyoung, "On visual similarity based 3D model retrieval", *Computer Graphics Forum (EG 2003 Proceedings)*, vol. 22, 2003.

[61] J.W.H. Tangelder and R.C. Veltkamp, "Polyhedral model retrival using weighted point sets", *International Journal of Image and Graphics*, vol. 3, pp. 209-229, 2003.

[62] S. Ruiz-Correa, R.W. Sze, J.R. Starr, H.J. Lin, M.L. Speltz, M.L. Cunningham, and A.V. Hing, "New scaphocephaly severity indices of sagittal craniosynostosis: A comparative study with cranial index quantifications", *Clef Palate Craniofacial Journal*, vol. 43, pp. 211-221, 2006.

[63] N. Iyer, S. Jayanti, K. Lou, Y. Kalyanaraman, and K. Ramani, "Three dimensional shape searching: State-of-the-art review and future trends", *Computer-Aided Design*, vol. 37, pp. 509-530.

[64] J.W.H. Tangelder and R.C. Veltkamp, "A survey of content based 3D shape retrieval methods", *Proc. Shape Modeling International 2004 (SMI '04)*, vol. , pp. , 2005.

[65] P.J. Besl and N.D. McKay, "A method for registration of 3-d shapes", *IEEE Trans. PAMI*, vol. 14, pp. 239-256, Feb. 1992.

[66] M. Austin-Seymour, G.T.Y Chen, J. Rosenman, J. Michalski, K. Lindsley and M. Giotein, "Tumor and target delineation: current research and future challenges", *International Journal of Radiation Oncology, Biology and Physics*, vol. 33, pp. 1073-1080, 1995.

[67] C. Teng, L.G. Shapiro, I. Kalet, C. Rutter, and R. Nurani "Head and neck cancer patient similarity based on anatomical structural geometry", *Proc. 2007 IEEE International Symposium on Biomedical Imaging*, in press.

[68] D.J. Hawkes, and D.L.G. Hill, "Medical imaging at Guy's Hospital, King's College London", *IEEE Trans. Medical Imaging*, vol. 22, no. 9, pp. 1033-1041, Sep. 2003.

[69] J. Barker, M. Austin-Seymour, I. Kalet, M. Whipple, C. Teng, and L.G. Shapiro, "Automated delineation of regional target volume for patients with head and neck cancer treated conformally", *International Journal of Radiation Oncology, Biology and Physics*, vol. 54, no. 2, supplement, pp. 15, Oct. 2002.

[70] N. Benson, M. Whipple and I.J. Kalet, "A Markov Model Approach to Predicting Regional Tumor Spread in the Lymphatic System of the Head and Neck," *Proceedings of the American Medical Informatics Association Fall Symposium*, pp. 31-35, Nov. 2006.

[71] S. Ruiz-Correa, R.W. Sze, H.J. Lin, L.G. Shapiro, M.L. Speltz, and M.L. Cunningham, "Classifying Craniosynostosis Deformations by Skull Shape Imaging", *Proceedings of the 18th IEEE Internatioanl Symposium on Computer-Based Medical Systems*, pp. 335-340, 2005.

[72] S. Ruiz-Correa, R.W. Sze, J.R. Starr, A.V. Hing, , and M.L. Cunningham, "A Fourier-based approach for quantifying sagittal synostosis head shape", *American Cleft Palate-Craniofacial Association Meeting*, 2005.

[73] H.J. Lin, S. Ruiz-Correa, L.G. Shapiro, A.V. Hing, M.L. Cunningham, M.L. Speltz, and R.W. Sze, "Symbolic shape descriptors for classifying craniosynostosis deformations from skull imaging", *Engineering in Medicine and Biology Society 2005. IEEE EMBS 2005. 27th Annual International Conference of the*, pp. 6325-6331, 2005.

[74] S. Kullback and R. Leibler. On information and suciency. *Ann. Math. Stat.*, vol. 22, pp. 79-86, 1951.

VITAE

Chia-Chi Teng

Education:

- National Tsing Hua University, Hsinchu, Taiwan, B.S., Electrical Engineering, 1985.
- University of Washington, Seattle, Washington, M.S., Electrical Engineering, 1993.
- University of Washington, Seattle, Washington, Ph.D., Electrical Engineering, 2007.

Services:

- Second Lieutenant, Chinese Marine Corp, Kaohsiung, Taiwan, Republic of China, 1985-1987
- Missionary, Taichung Taiwan Mission, The Church of Jesus Christ of Latter-Day Saints, 1987-1989

Honor:

- Valedictorian, ROTC Class of 1985, Chinese Marine Corps Institute, Kaohsiung, Taiwan, Republic of China, 1985

Research and Development Positions Held:

- Institute of Information Systems and Applications, National Tsing Hua University, Research Assistant, 1985
- Microsoft Corporation, 1989-2005:
  Printer Business Unit, Software Design Engineer, 1989-1992
  Windows 95© Development, Software Design Engineer Lead, 1992-1995
  Internet Explorer© Development, Software Design Engineer Lead, 1995-1997
  Microsoft Research, Software Design Engineer Lead, 1997-1998
  Microsoft Network MSN©, Development Manager, 1998-2000
  Microsoft TV Division, Software Development Engineer Lead, 2000-2002
  Windows Vista© Development, Software Design Engineer Lead, 2002-2005

Patents:

1. L.F. Shaw, **C. Teng**, K.W. Sykes, and R.E. Endres, "Device Independent Spooling in a Print Architecture," US Patent 5602974, Oct. 1994.
2. J.E. Marbry, S.J. McKelvie, D.H. Tryon, L.F. Shaw, and **C. Teng**, "Automatic Installation of Printers in a Distributed Environment," US Patent 5692111, Apr. 1996.
3. L.F. Shaw, **C. Teng**, K.W. Sykes, and R.E. Endres, "Device Independent Spooling in a Print Architecture," US Patent 5845058, Nov. 1996.
4. L.F. Shaw, **C. Teng**, K.W. Sykes, and R.E. Endres, "Deferred Printing," US Patent 5881213, Oct. 1997.
5. L.F. Shaw, **C. Teng**, K.W. Sykes, and R.E. Endres, "Deferred Printing," US Patent 5960168, Dec. 1998.
6. **C. Teng**, and B. Jahromi, "Distribution of Software in a Computer Network Environment," US Patent 6094679, Jan. 1998.
7. **C. Teng**, and B. Jahromi, "System and Method for Collecting Printer Administration Information," US Patent 6240456, Sep. 1997.
8. **C. Teng**, and B. Jahromi, "Computer Network," US Patent 6327045, Sep. 1997.
9. R.M. Fries, and **C. Teng**, "Interactivity Emulator for Broadcast Communication," US Patent Application Pub. No. 20030221197, Nov. 2003.
10. G.A.Z. Perkins, W.J. Tutt, **C. Teng**, and T.E. Wood, "Electronic Registration Manager for Business Directory Information," US Patent Application Pub. No. 20040204958, Oct. 2004.
11. C.H. Shoemaker, **C. Teng**, H.C. Vidos, and J.C. Gibson, "Systems and Methods for Determining Remote Device Media Capabilities," US Patent Application Pub. No. 20050080915, Apr. 2005; European Patent Application Pub. No. 1521427, Jun. 2005.

Referred Conference Proceedings:

1. **C. Teng**, M. Austin-Seymour, J. Barker, I. Kalet, L.G. Shapiro and M. Whipple, "Head and Neck Lymph Node Region Delineation 3-D CT Image Registration," *Proceedings of the American Medical Informatics Association (AMIA) Fall Symposium*, pp. 767-771, November 2002.

2. **C. Teng**, L.G. Shapiro, and I. Kalet, "Head and neck lymph node region delineation using a hybrid image registration method," *Proceedings of the 3rd IEEE International Symposium on Biomedical Imaging (ISBI)*, pp. 462-465, April 2006.

3. **C. Teng**, L.G. Shapiro, and I. Kalet, "Automatic segmentation of neck CT images," *Proceedings of the 19th IEEE International Symposium on Computer-Based Medical Systems (CBMS)*, pp. 442-445, June 2006.

4. **C. Teng**, L.G. Shapiro, I. Kalet, C. Rutter, and R. Nurani "Head and neck cancer patient similarity based on anatomical structural geometry," *Proceedings of the 4th IEEE International Symposium on Biomedical Imaging (ISBI)*, in press, April 2007.

Abstract Published:

1. J. Barker, M. Austin-Seymour, I. Kalet, M. Whipple, **C. Teng**, and L.G. Shapiro, "Automated Delineation of Regional Target Volumes for Patients with Head and Neck Cancer Treated Conformally," *International Journal of Radiation Oncology, Biology and Physics*, Volume 54, Number 2, Supplement, pp. 15, October 2002.